Multipoint aerodynamic design of ultrashort nacelles for ultrahigh-bypass-ratio engines

Multipoint Aerodynamic Design of Ultra-short Nacelles for Ultra-high Bypass Engines

Vinícius T. Silva *
Chalmers University of Technology, 412 58 Gothenburg, Sweden

Anders Lundbladh †
GKN Aerospace, 461 81 Trollhättan, Sweden.

Olivier Petit‡
LFV Operations, 438 80 Landvetter, Sweden

Carlos Xisto§
Chalmers University of Technology, 412 58 Gothenburg, Sweden.

This paper presents a newly developed methodology for multipoint aerodynamic design of ultra-short nacelles for ultra-high bypass ratio turbofan engines. An integrated aerodynamic framework, based on parametric geometry generation and flow field solution via three-dimensional Reynolds-Averaged Navier-Stokes equations, was built and used for designing several ultra-short nacelle shapes and to evaluate their aerodynamic performance. An approach for estimating the static pressure distribution at the fan face, based on the parallel compressor theory, is presented and validated. A design strategy is introduced and various test cases are evaluated under the following critical operating conditions: mid-cruise, low speed/ high angle of attack, and pure crosswind. The major design parameters are highlighted and their influence in the flow field is discussed in detail for all the chosen flight conditions. Performance was evaluated by assessing inlet flow distortion and by bookkeeping of thrust and drag. The framework has proven to be suitable for designing high performance nacelles capable of operating under critical flight conditions, without flow separation or high levels of distortion. Drooping the inlet by 4 degrees is shown to reduce the drag at cruise by 1.9%, which also has a large beneficial impact on internal lip separation at high incidence conditions. Furthermore, crosswind was identified as the most severe of the conditions, requiring a drastic reshaping of the nacelle to avoid internal lip separation. Two final nacelle designs were compared: the first allowing inlet separation under a 90-degree crosswind condition, whilst the second was reshaped to be separation-free under all operating conditions. Reshaping to avoid separation

*PhD Candidate, Mechanics and Maritime Sciences, Chalmers University of Technology, Hörsalsvägen 7A, 412 58 Gothenburg, Sweden.
†Specialist Whole Engine, Engine Systems, GKN Aerospace, Flygmotorvägen 1, 461 81 Trollhättan, Sweden.
‡Performance Specialist, Environment and Performance Group, LFV Operations, 438 80 Landvetter, Landvetter airport, Sweden
§Associate Professor, Mechanics and Maritime Sciences, Chalmers University of Technology, Hörsalsvägen 7A, 412 58 Gothenburg, Sweden.

has increased drag by 5.1% at cruise.

Nomenclature

Roman Letters

A_{fan}	=	Fan face area
a	=	Lip length
BP_n	=	Bernstein polynomial of order n
b	=	Lip height
bp_i	=	Bernstein weighing coefficients
c_p	=	Specific heat for constant pressure
c_v	=	Specific heat for constant volume
$C(\psi)$	=	Class function
C_D	=	Drag coefficient
$C_{l_{max}}$	=	Maximum lift coefficient
C_p	=	Pressure coefficient
c	=	Chord
DC_{60}	=	Total pressure distortion parameter
D_c	=	Configuration drag
Φ_{FC}	=	Fan cowl force
d_{fan}	=	Fan diameter
e	=	Specific internal energy
E	=	Total energy
Φ_{scrub}	=	Scrubbing force
F_N	=	Net propulsive force
F_{pre}	=	Pre-entry force
f_{cpr}	=	Lip control point radial position
f_{cpx}	=	Lip control point axial position
f_{le}	=	Non-dimensional leading edge radius of curvature
F	=	Blending factor in the $k-\omega$ SST model
h	=	equivalent mesh size
H	=	Total enthalpy
k	=	Turbulence kinetic energy

$K_{i,n}$	=	Binomial coefficients
$\mathcal{K}$	=	Constant in the $k-\omega$ SST model
L	=	Length
$\dot{m}$	=	Mass flow
M	=	Mach number
M_{is}	=	Isentropic Mach number
M_{max}	=	Maximum Mach number in a flow field
N	=	Number of elements in a mesh
$\overline{P}_{02,60}$	=	Average total pressure at a 60-degree sector
$\overline{P}_{02}$	=	Average total pressure at the fan face
p	=	Static pressure
Pr_l	=	Laminar Prandtl number
Pr_t	=	Turbulent Prandtl number
PR	=	Pressure Ratio
q_{l_j}	=	Laminar mean heat-flux vector
q_{t_j}	=	Turbulent mean heat-flux vector
r	=	Radius
R	=	Radius of curvature
S	=	Bookkeeping boundary surfaces
$S(\psi)$	=	Shape function
T	=	Static temperature
T_0	=	Total temperature
T_N	=	Standard net thrust
f_h	=	Discrete numerical solution
f_e	=	Extrapolated solution
$\vec{i}$	=	Axial unity vector
$\vec{n} = [n_x, n_y, n_z]$	=	Normal vector
$\overline{q}$	=	Average dynamic pressure
u_i	=	Velocity in tensor notation
$\vec{V} = [u, v, w]$	=	Velocity in vector notation
x, r, ϕ	=	Cylindrical coordinates

Greek Letters

β_{te}	=	Nacelle boattail angle
δ_{ij}	=	Kronecker delta
ϵ	=	Estimated relative error
η_{is}	=	Isentropic efficiency
μ	=	Dynamic viscosity
μ_t	=	Dynamic eddy viscosity
ν_t	=	Kinematic eddy viscosity
$\phi_{m,corr}$	=	Corrected mass flux
ρ	=	Density
τ_{ij}	=	Viscous stress tensor
τ_{ij}^R	=	Reynolds stress tensor
$\vec{\tau}_x = [\tau_{xx}, \tau_{xy}, \tau_{xz}]$	=	Axial viscous stress in vector notation
θ_d	=	Droop angle
ζ	=	Sutherland Temperature

Subscripts

0	=	Captured streamtube station
1	=	Inlet station
13	=	Fan outlet station
18	=	Bypass nozzle exhaust station
2	=	Fan face station
8	=	Core nozzle exhaust station
BN	=	Bypass nozzle
CC	=	Core cowl
CN	=	Core nozzle
FC	=	Fan cowl
I	=	Inlet
P	=	Plug
S	=	Spinner
hi	=	Highlight
max	=	Position of maximum radius
ref	=	Reference
te	=	Trailing edge

th = Throat

∞ = Freestream

I. Introduction

In the pursuit of reduced fuel burn and emissions, the next generation of turbofan engines for civil aircraft will be designed for a higher bypass ratio (BPR) and lower fan pressure ratio (FPR). Future aero-engines are expected to operate with cruise FPR below 1.4, possibly leading to bypass ratios above 15, referred to as ultra-high bypass ratio (UHBPR), in order to achieve reduced specific thrust and higher propulsive efficiency. These configurations require large fan diameters and are likely to be accompanied by increased weight and drag. Therefore, advanced nacelle designs, with shorter inlets and exhaust nozzles, are required so that the achieved performance benefits are not outweighed by the increased installation drag and propulsion system weight.

Current engines for long range twin-engine aircraft feature inlets with lengths over fan diameter ratios L_I/d_{fan} between 0.5 and 0.65. To minimize drag and weight, 2030+ airplanes are expected to have inlets with L_I/d_{fan} considerably below 0.5. The design of such short inlets can be highly challenging, especially for low speed and high incidence conditions, since they have reduced internal diffusion capability and boundary layer separation is likely to occur, leading to poor performance and engine instability.

Considerable achievements in modern nacelle design were reached over the last decade. Christie, et al. [1], and Christie, et al. [2] have developed new Class Shape Transformation (CST) based approaches for designing nacelle and intake aero-lines. Tejero, et al. [3] and Tejero, et al. [4] have developed CST based methods for 3D nacelle shape multi-objective optimization. Furthermore, CST curves were also widely used for designing inlets [5–8] and for exhaust nozzles design and optimization [9–11]. However, to the knowledge of the authors, the presented CST methodologies for designing 3D nacelle shapes considered only flight conditions under the cruise segment, and thus neglecting other critical conditions within the flight envelope. Therefore, the CST method capability was not yet explored for designing 3D asymmetric geometries capable of performing well under the most critical flight conditions. Besides, the CST method was not yet applied to the design of ultra-short nacelles, with L_I/d_{fan} below 0.4.

Peters, et al. [12] have presented a spline-based framework for designing nacelles with ultra-short inlets and assessed the performance of different short inlet candidates compared to a standard-length baseline. It was found that, for inlets with $L_I/d_{fan} < 0.25$, the benefit from reduced nacelle drag is offset by the reduction in fan efficiency and, based on a parametric study, they suggested that the optimum L_I/d_{fan} is between 0.25 and 0.4. Schnell and Corroyer [13] presented a coupled fan-intake design methodology for potential application to ultra-short intakes for UHBPR engines and concluded that the fan efficiency could be retained when shortening the intake at different flow conditions. To the extent of the authors' knowledge, these are the only articles available in literature which address the design of ultra-short

nacelles.

Extensive research has been conducted on nacelles subjected to high incidence [1, 12, 14] and crosswinds [15–18]. Although some studies considering crosswind effects on short inlets exist [12, 13, 19], not much has been explored on how crosswind can impact the design of ultra-short nacelles. Furthermore, the design of nacelles with ultra-short inlets remains an under-exploited area, since not much can be found in the literature besides the work presented in [12, 13].

This paper is built on the aforementioned research, providing a novel CST based methodology for multipoint design of ultra-short nacelles. The design procedure considers 3D effects of both asymmetric geometries and asymmetric flow field under some of the most critical conditions of the aircraft mission, such as cruise, high angle-of-attack and crosswind. Moreover, a step further is achieved on the design of ultra-short nacelles, by a thorough assessment of the impact of the major design parameters on the flow field for the selected operating conditions.

II. Methodology

The shape of a nacelle is a compromise to satisfy conflicting requirements for different operating conditions. At cruise, the aim is to minimize drag. Therefore, shock waves outside of the fan cowling should be avoided, since they are accompanied by a significant increase in wave drag. At low-speed and high-incidence conditions, such as end of take-off, initial climb and crosswind, the main design focus is to prevent boundary layer separation inside the inlet. Therefore, the design efforts presented in this article are towards minimizing the super-velocities at the external nacelle surface during cruise while maintaining the inlet boundary layer fully attached for the low-speed/ high-incidence critical conditions. The following sections present a brief overview of the methodology utilized to design nacelles and evaluate their aerodynamic performance.

A. Geometry Generation

This subsection will cover the methods used for generating the nacelle's geometry. Here the CST method and the major design parameters will be addressed.

1. Class Shape Transformation Method

The Class Shape Transformation (CST) method [20, 21] has shown to be a robust and versatile approach for parametric geometry representation, allowing the construction of smooth shapes with a limited amount of design variables. It consists of the product between a class function $C(\psi)$ and a shape function $S(\psi)$, that can be mathematically represented as follows:

$$\xi(\psi) = S(\psi)\, C(\psi) + \psi \Delta\xi_{te} \tag{1}$$

where $\xi = r/c$, $\psi = x/c$ and the term $\psi\Delta\xi_{te}$ is added to modify the trailing edge's radial coordinate. The class function determines the basic profile, which can be written as

$$C(\psi) = \psi^{N1}(1-\psi)^{N2} \tag{2}$$

The exponents N_1 and N_2 in Eq. (2) are used to mathematically define the class of the geometric shape. For a round nose and a sharp trailing edge, $N_1 = 0.5$ and $N_2 = 1$. The shape function is used to transform the class function and can be represented by a nth order Bernstein polynomial, defined as

$$BP_n(\psi) = \sum_{i=0}^{n} \left[K_{i,n} \cdot \left(\psi^i (1-\psi)^{n-i} \right) \right] \tag{3}$$

where $K_{i,n}$ are the binomial coefficients

$$K_{i,n} = \frac{n!}{i!(n-i)!} \tag{4}$$

The shape function can be generated by multiplying Eq.(3) by weighting coefficients bp_i, acquiring the following form

$$S(\psi) = \sum_{i=0}^{n} \left[bp_i \cdot K_{i,n} \cdot \left(\psi^r (1-\psi)^{n-i} \right) \right] \tag{5}$$

The first weighting coefficient bp_0 is directly related to the airfoil leading-edge radius of curvature R_{le} by the relation

$$bp_0 = \sqrt{\frac{2R_{le}}{c}} \tag{6}$$

whilst the last weighting coefficient bp_n is related to the boattail angle and trailing edge radial offset, as follows

$$bp_n = \tan(\beta_{te}) + \frac{\Delta\xi_{te}}{c} \tag{7}$$

In order to calculate the remaining weighting coefficients and hence to fully define $\xi(\psi)$, a set of constraints must be defined, which can be either control points or derivatives. Once these constraints are specified, a $(n-1)$ by $(n-1)$ linear set of equations is formed from Eq. (1) and its derivatives $\xi(\psi)'$ and $\xi(\psi)''$. By solving this system, the CST curves are determined.

2. Ultra-Short Nacelle Parametrization

A full 2D nacelle geometry is defined by joining six different CST curves, representing the inlet, fan cowl, bypass and core nozzle outer parts, core cowl, core nozzle and plug. Figure 1 shows the main geometric parameters for the inlet and fan cowling geometric representation and Table 1 depicts the main input design parameters. The design procedure

described in this paper will focus on the inlet and fan cowl design, therefore details about the bypass and core nozzles will not be addressed.

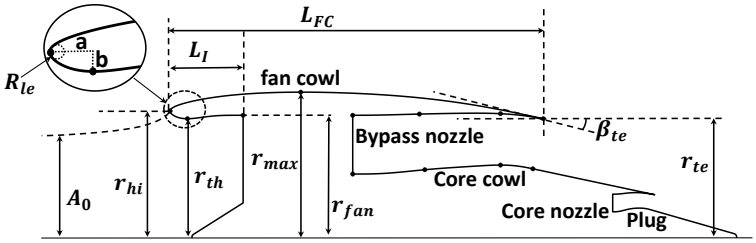

Fig. 1 Nacelle main geometric parameters.

Table 1 Fan cowl and inlet design parameters

Parameter	Description
Inlet length to fan diameter ratio	L_I/d_{fan}
Contraction ratio	r_{hi}^2/r_{th}^2
Lip aspect ratio	a/b
Highlight radius to maximum radius ratio	r_{hi}/r_{max}
Fan cowl length to maximum radius ratio	L_{FC}/r_{fan}
Trailing edge radius to fan radius ratio	r_{te}/r_{fan}
Maximum radius to fan radius ratio	r_{max}/r_{fan}
Axial position of maximum diameter	$f_{max} = x_{max}/L_{FC}$
Non-dimensional leading-edge radius of curvature	$f_{le} = \frac{R_{le} f_{max} L_{FC}}{(r_{max}-r_{hi})^2}$
Nacelle boattail angle	β_{te}
Inlet droop	θ_d
Lip control point axial position	$f_{cpx} = \frac{x_{cp}-x_{hi}}{a}$
Lip control point radial position	$f_{cpr} = \frac{r_{cp}-r_{hi}}{b}$

Figure 2 shows a 3D nacelle geometric definition. Two dimensional parametrizations are performed for the locations of $\phi = 0^o$, $\phi = 90^o$ and $\phi = 180^o$, referred to as crown, maximum half-breadth (MHB) and keel, where ϕ is the azimuth angle in a cylindrical coordinate system. In order to obtain a 3D nacelle shape, sinusoidal interpolations in r (radial coordinate) and x (axial coordinate) are performed circumferentially between the crown, MHB and keel. The second nacelle half ($180^o \leq \phi \leq 0^o$) is geometrically symmetric to the first one.

The previously mentioned parametrization positions were selected specifically to allow geometric control where local flow effects are critical. At the crown, the strongest shock waves are formed, whereas the keel geometry plays a fundamental role in preventing separation at high incidence and low-speed operational conditions. Furthermore, the MHB parametrization is important to prevent separation and minimize distortion under crosswind conditions. The

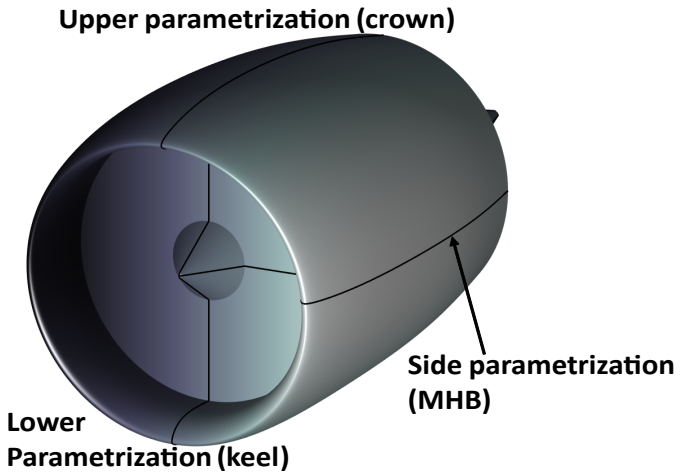

Fig. 2 Nacelle 3D geometry definition.

control point parameters f_{cpx} and f_{cpr} are used only for the MHB and keel, where local curvature control is desired to design a round lip.

An important characteristic existent in modern turbofan engines is a droop to align the inlet with the wing upwash at cruise [22]. However, it is not clear in the literature how such droop is performed. In this article, two methods for drooping the nacelle are presented and compared. In both, the crown and keel highlight positions are rotated around a pivoting point located at the intersection between the fan face plane and the engine centerline. A shape deformation function is then applied to the original CST curves so that the inlet and fan cowl shapes are stretched to the new drooped highlight position, proportionally to a quadratic function of the axial position.

In method 1, only the fan cowl forebody is stretched, so that the geometry downstream of the fan face remains unchanged. In method 2, the deformation is employed to the entire cowling. The major advantage with method 2 is to assure a gradual change in curvature for the fan cowl, keeping the smooth nature of the CST curves. On the other hand, method 1 allows the fan cowl afterbody to remain unchanged, which could be advantageous for designing an axisymmetric geometry downstream of the inlet. These methods will be compared later in this work. The drooping procedure is illustrated in Fig. 3.

A comparison between the range of design parameter values for conventional nacelles found in literature and the ones used for designing the ultra-short nacelles presented in the current work is shown in Table 2. It can be seen that the parameters L_I/d_{fan} and L_{FC}/r_{hi} fall off from the conventional range, as expected for ultra-short nacelles. Moreover, higher than usual lip aspect ratios (a/b) are necessary for achieving good low speed performance. The impact of several of the parameters presented in Table 2 on the design of ultra-short nacelles will be discussed later in this work.

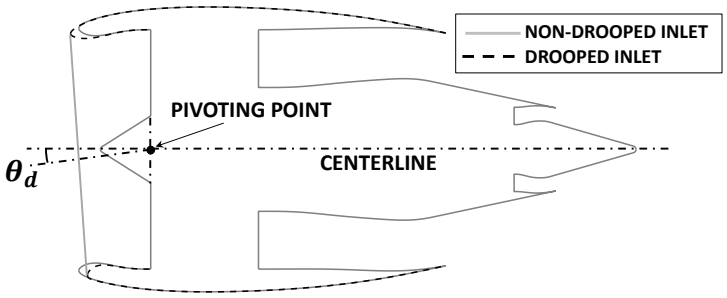

Fig. 3 Drooped inlet representation.

Table 2 Range of values for nacelle design parameters – conventional nacelle design compared with the present work

Parameter	Literature	Present work
L_I/d_{fan}	0.5 – 0.85 [12]	0.3
r_{hi}^2/r_{th}^2	1.1 – 1.3 [23]	1.135 – 1.25
a/b	1.5 – 3.0 [12, 24]	1.19 – 5.0
r_{hi}/r_{max}	0.75 – 0.91 [4, 12, 23, 24]	0.85 – 0.89
r_{te}/r_{hi}	0.89 – 1.0 [4]	0.94
L_{FC}/r_{hi}	3.1 – 6.49 [8, 25]	2.96
f_{max}	0.25 – 0.51 [4, 23]	0.24 – 0.35
f_{le}	0.6 – 1.4 [3, 4]	0.75 – 1.2
β_{te} $(^o)$	9 – 15 [3, 4]	10 – 13
θ_d $(^o)$	3 – 6 [12, 22]	4 – 5

B. Numerical Approach

Multiblock structured meshes are automatically generated using the ANSYS ICEM CFD meshing software. They are defined within a computational domain between the nacelle and a cylindrical far-field, with length and diameter equal to 60 times the fan diameter. In order to resolve the viscous sub-layer, the first cell height was set so that $y^+ < 1$ for the cruise condition. Figure 4 shows an example of the 3D mesh.

The flow field around the nacelle was computed by the means of computational fluid dynamics (CFD). The commercial software ANSYS FLUENT was used as the CFD solver. The simulations were performed for the Reynolds-Averaged Navier-Stokes (RANS) equations, using the pressure-based solver and the pressure-velocity coupled algorithm [26]. The chosen turbulence closure model was the Menter's $k-\omega$ shear stress transport (SST) model [27], since it has been proven to be suitable for external compressible aerodynamic computations [28, 29], furthermore, it has been used multiple times for computing the aerodynamic performance of high bypass turbofan nacelles and exhaust nozzles [3–5, 7, 11]. The least squares cell-based method was used for computation of the flow field gradients and a second order upwind scheme was employed to interpolate the convection terms along with the specific dissipation rate and the

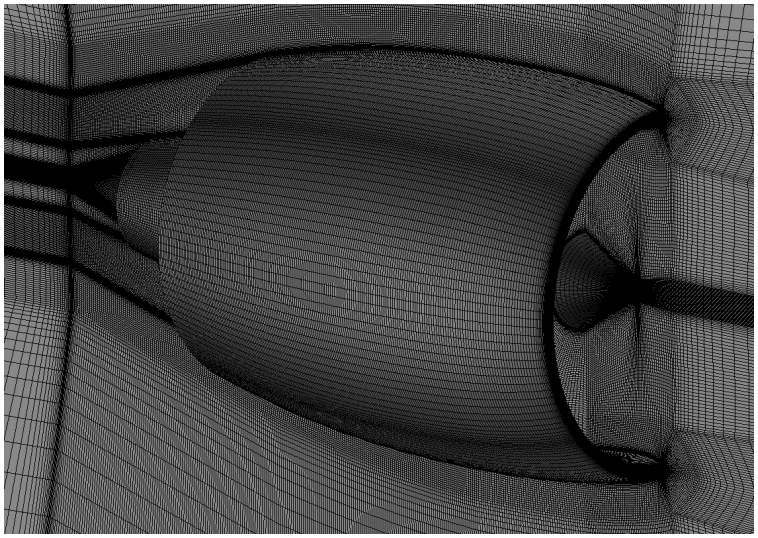

Fig. 4 Nacelle 3D multiblock sturctured mesh.

turbulence kinetic energy. Both 2D axisymmetric and 3D computations are necessary in order to fulfill the entire nacelle design procedure, however, the focus will be on the latter. The 2D simulations are used as a tool to find a preliminary nacelle design with low computational cost. The obtained geometry is used as a starting point for the 3D computations. Details on the governing equations and boundary conditions utilized in the 3D CFD simulations are presented next.

1. Governing Equations

The Reynolds form of the continuity, momentum and energy equations, for a compressible flow, often referred to as RANS equations, in mass-weighted averaged variables, can be written respectively as

$$\frac{\partial \overline{\rho}}{\partial t} + \frac{\partial}{\partial x_i}\left(\overline{\rho}\tilde{u}_i\right) = 0 \tag{8}$$

$$\frac{\partial}{\partial t}\left(\overline{\rho}\tilde{u}_i\right) + \frac{\partial}{\partial x_j}\left(\overline{\rho}\tilde{u}_j\tilde{u}_i\right) = -\frac{\partial \overline{p}}{\partial x_i} + \frac{\partial}{\partial x_j}\left(\overline{\tau}_{ji} - \overline{\rho u_j'' u_i''}\right) \tag{9}$$

$$\frac{\partial}{\partial t}(\bar{\rho}E) + \frac{\partial}{\partial x_j}\left(\tilde{u}_j(\overline{\rho}E + \overline{p})\right) = \frac{\partial}{\partial x_j}\left[-q_{l_j} - q_{t_j} + \overline{\tau_{ji}u_i''} - \frac{1}{2}\overline{\rho u_j'' u_i'' u_i''}\right] + \frac{\partial}{\partial x_j}\left[\bar{u}_i\left(\bar{\tau}_{ij} - \overline{\rho u_i'' u_j''}\right)\right] \tag{10}$$

where E is the total energy, τ_{ij} is the viscous stress tensor, and q_{l_j} and q_{t_j} are the laminar and turbulent mean heat-flux vectors, respectively. The superscript symbols $\tilde{}$ and $\bar{}$ represent, respectively, mass-weighted and unweighted averaged variables. Double primes indicate fluctuating parts of field variables, from a Favre decomposition. The total energy can be defined as a function of the Favre-averaged specific internal energy $\tilde{e}$, as follows

$$E = \tilde{e} + \frac{1}{2}\tilde{u}_i\bar{u}_i + k \tag{11}$$

where k is the turbulence kinetic energy, $\frac{1}{2}\widetilde{u_i''u_i''}$. The mean viscous stress tensor $\overline{\tau}_{ij}$ can be written as in Eq. 12:

$$\overline{\tau}_{ij} = \mu\left[\left(\frac{\partial\tilde{u}_i}{\partial x_j} + \frac{\partial\tilde{u}_j}{\partial x_i}\right) - \frac{2}{3}\delta_{ij}\frac{\partial\tilde{u}_k}{\partial x_k}\right] \tag{12}$$

where μ is the dynamic viscosity and δ_{ij} is the Kronecker delta. The term $-\overline{\rho u_i'' u_j''}$, referred to as Reynolds stress tensor τ_{ij}^R, is modeled using the Boussinesq hypothesis, as shown in Eq. (13):

$$\tau_{ij}^R = \mu_t\left(\frac{\partial\tilde{u}_i}{\partial x_j} + \frac{\partial\tilde{u}_j}{\partial x_i}\right) - \frac{2}{3}\left(\overline{\rho}k + \mu_t\frac{\partial\tilde{u}_k}{\partial x_k}\right)\delta_{ij} \tag{13}$$

where μ_t is the eddy viscosity. The laminar and turbulent heat-flux vectors are computed as follows

$$q_{l_j} = -\frac{\mu c_p}{Pr_l}\frac{\partial\tilde{T}}{\partial x_j} \tag{14}$$

$$q_{t_j} = -\frac{\mu_t c_p}{Pr_t}\frac{\partial\tilde{T}}{\partial x_j} \tag{15}$$

where Pr_l and Pr_t are the laminar and turbulent Prandtl numbers, respectively. The term $\overline{\tau_{ji}u_i''}$ corresponds to the molecular diffusion and $\frac{1}{2}\overline{\rho u_j'' u_i'' u_i''}$ represents the turbulent transport of turbulence kinetic energy. The most commonly used closure approximation to model these terms is

$$\overline{\tau_{ji}u_i''} - \frac{1}{2}\overline{\rho u_j'' u_i'' u_i''} = \left(\mu + \frac{\mu_t}{\sigma_k}\right)\frac{\partial k}{\partial x_j} \tag{16}$$

where σ_k is a coefficient associated with the modelling of the turbulence kinetic energy equation.

The $k-\omega$ SST model was developed by Menter [27] to effectively blend the $k-\omega$ and $k-\epsilon$ formulations. The former is known to behave better in the inner parts of the boundary-layer whereas the latter is more suitable for the free-stream. The $k-\omega$ SST transport equations are solved to obtain the turbulence kinetic energy k and the specific dissipation rate ω:

$$\frac{\partial}{\partial t}(\overline{\rho}k) + \frac{\partial}{\partial x_j}\left(\overline{\rho}k\tilde{u}_j\right) = \tau_{ij}^R\frac{\partial\tilde{u}_i}{\partial x_j} - \overline{\rho}\beta^*\omega k + \frac{\partial}{\partial x_j}\left[\left(\mu + \frac{\mu_t}{\sigma_k}\right)\frac{\partial k}{\partial x_j}\right] \tag{17}$$

$$\frac{\partial}{\partial t}(\overline{\rho}\omega) + \frac{\partial}{\partial x_j}\left(\overline{\rho}\omega\tilde{u}_j\right) = \frac{\alpha}{\nu_t}\tau_{ij}^R\frac{\partial\tilde{u}_i}{\partial x_j} - \overline{\rho}\beta\omega^2 + \frac{\partial}{\partial x_j}\left[\left(\mu + \frac{\mu_t}{\sigma_\omega}\right)\frac{\partial\omega}{\partial x_j}\right] + 2\left(1-F_1\right)\overline{\rho}\frac{1}{\omega\sigma_{\omega,2}}\frac{\partial k}{\partial x_j}\frac{\partial\omega}{\partial x_j} \tag{18}$$

The kinematic eddy viscosity, $\nu_t = \mu_t/\rho$, is computed as follows

$$\nu_t = \frac{a_1 k}{\max(a_1\omega, SF_2)} \tag{19}$$

The model constants α, β, σ_k, σ_ω are obtained from a linear combination of the constants from the underlying $k-\epsilon$ and $k-\omega$ turbulence models, defined by Eq. (20)

$$\mathcal{K} = F_1\mathcal{K}_1 + (1 - F_1)\,\mathcal{K}_2 \tag{20}$$

where $\mathcal{K}_1$ represents any constant from the $k-\omega$ model, $\mathcal{K}_2$ is any constant from the $k-\varepsilon$ model, and $\mathcal{K}$ any constant from the $k-\omega$ SST model. F_1 and F_2 are blending functions, based on the distance from the nearest surface and on flow field variables, and S is the strain rate magnitude. The remaining model constants are: $a_1 = 0.31$, $\beta^* = 0.09$, and $\sigma_{\omega,2} = 1.168$. Further details on the $k-\omega$ SST model can be found in Refs. [26, 27].

The working fluid is air throughout the entire computational domain. It was modeled using the ideal gas law, therefore, pressure, density and temperature are related by

$$\overline{p} = \overline{\rho} R \tilde{T} \tag{21}$$

the specific gas constant R for air is $287.06\,J/(kg\cdot K)$. Moreover, the fluid is assumed to be calorific perfect and the internal energy can be expressed as a function of the specific-heat for constant volume c_v:

$$\tilde{e} = c_v \tilde{T} \tag{22}$$

The specific heats for constant volume c_v and for constant pressure c_p are related by

$$c_v = c_p - R \tag{23}$$

and c_p is computed by an 8th order polynomial of the following form

$$c_p = a_1 + a_2\tilde{T} + a_3\tilde{T}^2 + a_4\tilde{T}^3 + a_5\tilde{T}^4 + a_6\tilde{T}^5 + a_7\tilde{T}^6 + a_8\tilde{T}^7 \tag{24}$$

whose coefficients are shown in Table 3.

The Sutherland's law [30] was applied to compute the dynamic viscosity, defined by the following expression

$$\mu = \mu_{ref}\left(\frac{T}{T_{ref}}\right)^{3/2}\frac{T_{ref}+\zeta}{T+\zeta} \tag{25}$$

Table 3 Coefficients for computation of c_p

Polynomial coefficients	
a_1	1161.482
a_2	−2.368819
a_3	0.01485511
a_4	$-5.034909 \times 10^{-05}$
a_5	9.92857×10^{-08}
a_6	$-1.111097 \times 10^{-10}$
a_7	6.540196×10^{-14}
a_8	$-1.573588 \times 10^{-17}$

where $T_{ref} = 273.15\,K$, $\mu_{ref} = 1.716 \times 10^{-5}\,kg/(m \cdot s)$, and ζ, the Sutherland temperature, is equal to $110.4\,K$.

2. Boundary Conditions

The schematic representation of the CFD domain and boundary conditions (BC) for the 3D simulations is shown in Figs. 5a and 5b. A pressure outlet BC was set at the fan face, where the static pressure profile was specified. Mass flow is targeted to assure mass flow continuity between the fan and nozzles. At the fan and low-pressure turbine (LPT) outlets, mass flow inlet BCs were determined, where mass flow and total temperature were specified. For simulating crosswind operating conditions, the external far-field surface had to be split in 2. One half was modeled using a pressure-inlet BC, where total pressure and total temperature are specified, whilst the other was set to be a pressure-outlet BC, where static pressure profile was specified (see Fig. 5b). For all the remaining cases a pressure-far-field BC was used, where freestream static temperature, static pressure, Mach number and flow direction were specified (see Fig. 5a). All the nacelle surfaces were defined as non-slip adiabatic walls. The spinner was treated as a rotating wall. The freestream conditions, based on the International Standard Atmosphere (ISA), are described later in this work for each of the established operating points (see section II.E). The numerical approach used in this paper is summarized in Table II.B.

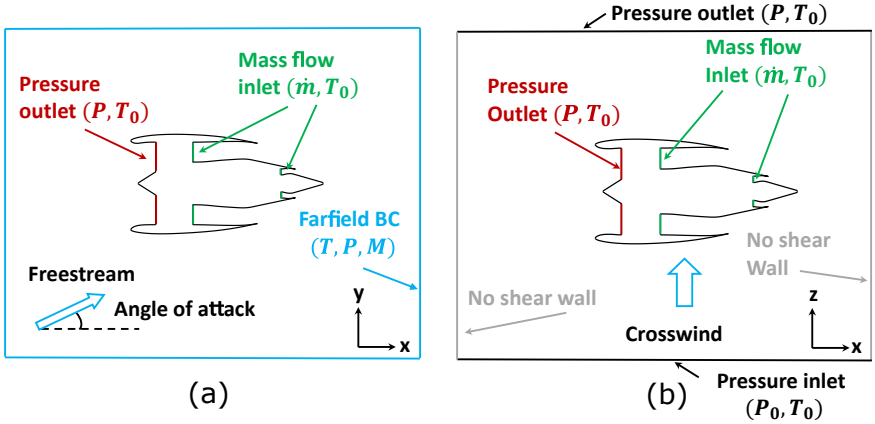

Fig. 5 Boundary conditions and CFD domain schematic representation for (a) cruise and high angle of attack, and (b) crosswind.

Table 4 Numerical approach used in this paper

Solver (ANSYS FLUENT)	3D RANS Pressure-based coupled; double precision
Boundary conditions	Viscous walls (no-slip); pressure outlet (p profile); mass flow inlet ($\dot{m}$, T_0) ; farfield (p, M, T)
Fluid type	Air modeled as an ideal gas; c_p as function of the static temperature; viscosity from Sutherland's law [30]
Spacial discretization	Second-order upwind; least squares cell based
Turbulence modelling ($y^+ < 1$)	$k - \omega$ SST

3. Fan Face Boundary Condition

Sometimes, during the preliminary stage of the engines' inlet design, the aerodynamicist might have limited or no access to the fan geometry. In such cases, simple and reliable boundary conditions are necessary to mimic the fan's behavior. Setting up a constant static pressure at the fan face would not capture properly the fan–inlet coupling and distortion effects. To overcome this problem, a methodology has been developed to calculate the static pressure profile at the fan face, based on the parallel compressor theory, which is a well-established method to estimate circumferential distortion effects on compressor performance. The method's intent is to be able to predict reasonably the fan's response to both clean and distorted incoming flows with a minimal amount of input data and low computational cost. Another goal is to be used as simple and robust alternative to to the existing body force models [31–33].

Cousins and Davis [34] present an historical overview of the parallel compressor theory and some of its variations, whilst Davis and Cousins [35] showed that the method can be applied to complex distortion patterns. The classical parallel compressor theory consists of dividing the compression system in two sectors. Both discharge to the same static pressure, but with different levels of inlet distortion, i.e., total pressure and temperature. Therefore, to reach a uniform outlet static pressure, the compressor with the lowest inlet total pressure has to operate with the highest pressure ratio, and vice versa. In other words, the fan works harder in the regions of lower energy. The consequence is that the lower the incoming total pressure, the lower the static pressure will be [36, 37]. This concept was adapted for CFD applications and used to compute the static pressure profile at the fan face, as described next.

An imaginary outlet plane is defined just downstream of the fan stator exit, where the flow is assumed to have uniform static pressure. The incoming flow field variables T_1, u_1, w_1, v_1 and $\dot{m}_1$, along with the cell face area A_1, computed from the CFD iteration, are used to calculate the stagnation pressure p_{01} and temperature T_{01}, using Eq. (26) to Eq. (29), for each grid point at the fan face, as follows:

$$V_1 = \sqrt{u_1^2 + v_1^2 + w_1^2} \tag{26}$$

$$M_1 = \frac{V_1}{\sqrt{\gamma R T_1}} \tag{27}$$

$$p_{01} = p_1 \left(1 + \frac{\gamma - 1}{2} M_1^2\right)^{\frac{\gamma}{\gamma-1}} \tag{28}$$

$$T_{01} = T_1 \left(1 + \frac{\gamma - 1}{2} M_1^2\right) \tag{29}$$

The corrected mass flux $\phi_{m,corr}$ is calculated as

$$\phi_{m,\text{corr}} = \frac{\dot{m}\sqrt{T_{01}/T_{0,\text{ref}}}}{A_1 \left(\frac{p_{01}}{p_{0,\text{ref}}}\right)} \tag{30}$$

and a compressor speed line is used to obtain the local pressure ratio PR and isentropic efficiency η_{is}. The speed line is linearized around the engine operating point, for improved numerical stability. The stagnation pressure and temperature are computed at the imaginary outlet plane as

$$p_{02} = p_{01} PR \tag{31}$$

$$T_{02} = T_{01} + \frac{T_{01}}{\eta_{is}} \left(PR^{\frac{\gamma-1}{\gamma}} - 1\right) \tag{32}$$

so that the outlet Mach number and static pressure can be calculated, through Eq. (33) and Eq. (34) , respectively.

$$\frac{\dot{m}\sqrt{R T_{02}}}{p_{02} A_2} = \sqrt{\gamma} M_2 \left(1 + \frac{\gamma - 1}{2} M_2^2\right)^{\frac{\gamma+1}{2(\gamma-1)}} \tag{33}$$

$$p_2 = \frac{p_{02}}{\left(1 + \frac{\gamma-1}{2} M_2^2\right)^{\frac{\gamma}{\gamma-1}}} \tag{34}$$

The outlet cell face area A_2 is obtained by assuming a constant area reduction ratio A_{ratio} between the fan entry and exit planes. Finally, the inlet static pressure is incremented by ΔP until a the outlet pressure p_2 is equal to a targeted pressure $p_{2,targ}$. The pressure increment ΔP can be calculated from Eq. (35), where λ is a weighting factor.

$$\Delta P = \lambda (p_{2,targ} - p_2) \tag{35}$$

This procedure is described in Fig. 6 and repeated for each one of the cells at the fan face. From now on, the method will be referred to as the modified parallel compressor (MPC) method. The target pressure can be determined by

using Eq. (33) and Eq. (34), with the stagnation pressure and temperature obtained from the engine cycle calculations. Particularly for the cases presented in this paper, there is a target for the cycle inlet mass flow, therefore, $p_{2,targ}$ must be iterated, to reach the target mass flow. Note that the only inputs necessary are: $p_{2,targ}$, A_{ratio}, and the compressor or fan speed-line. The method is designed so that a generic speed line can be utilized and scaled to the engine's operating point. The speed lines used for the nacelle CFD simulations, presented later in this work, were obtained from Ref. [38].

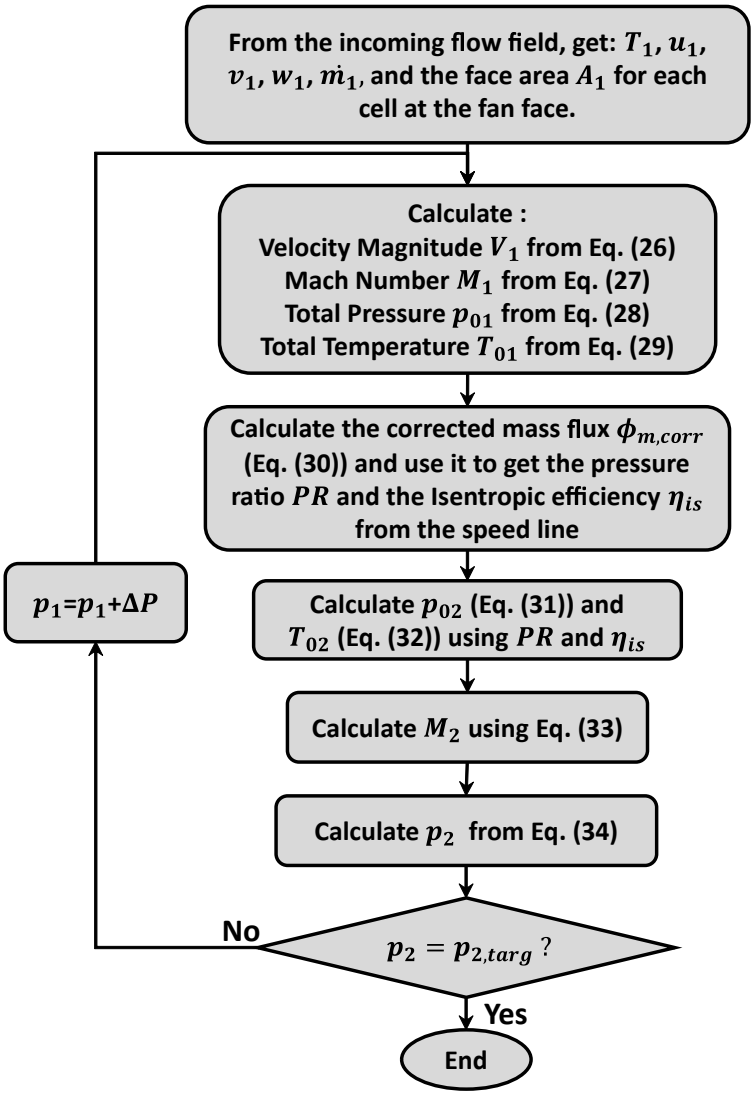

Fig. 6 Flowchart of the modified parallel compressor method.

The following assumptions and simplifications were made so that the MPC method could be developed: 1) each mesh element at the fan face is acting as a parallel compressor and there is no circumferential flow migration between different parallel compressors. Consequently, the area reduction ratio between the inlet and outlet planes becomes the same for all the elements; 2) there is no blockage caused by secondary flows at the blade tip clearance; 3) the use of a single speed line assumes that the fan has the same behaviour from the hub to the shroud. This approach captures

variations in radial work caused by distorted flows, but is incapable of predicting variations in work cased by the fan blade design; 4) the outlet static pressure is constant. The consequences of such assumptions as well as the MPC method limitations will be further further addressed in section III.B, where a validation is carried out.

C. Thrust and Drag Bookkeeping

Aerodynamic forces can be computed using either the body or the fluid flow perspective [39]. Methods employing the former are referred to as near-field and the latter as far-field. A modified near-field bookkeeping method, which involves integration both over the nacelle surfaces and along the captured streamtube, was used to calculate thrust, drag and assess the nacelle aerodynamic performance at cruise. Figure 7 shows the boundary surfaces used in the method to be described hereafter.

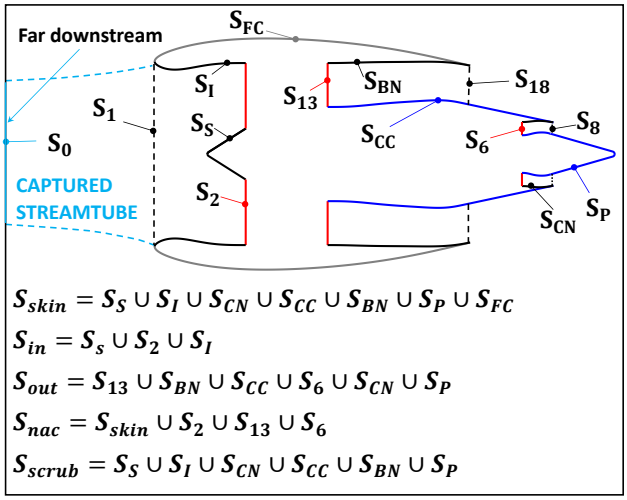

Fig. 7 Nacelle bookkeeping surfaces.

The near-field net propulsive force F_N can be determined from application of the axial momentum balance to a closed surface surrounding nacelle S_{nac} [40–43], as shown in Eq. (36).

$$F_N = -\int_{S_{\text{nac}}} \left[\rho\,(u-u_\infty)\,(\vec{V}\cdot\vec{n}) + (p-p_\infty)\,n_x - (\vec{\tau}_x\cdot\vec{n})\right] dS = \int_{S_{nac}} \left(\vec{f}\cdot\vec{n}\right)\, dS \tag{36}$$

where $\vec{f}$, following Destarac's [42] notation, is defined as:

$$\vec{f} = -\rho\,(u-u_\infty)\left(\vec{V}\cdot\vec{n}\right) - (p-p_\infty)\,\vec{i} + (\vec{\tau}_x\cdot\vec{n}) \tag{37}$$

The net propulsive force is defined as the difference between thrust and configuration drag D_c. Therefore, upon choosing one definition for thrust, D_c can be determined. The most commonly utilized definition in bookkeeping systems is the standard net thrust T_N [40–42, 44].

Classical methods [44] use the inlet entry and nozzles exit surfaces (S_1, S_{18} and S_8) to define thrust and drag, nevertheless, for CFD applications, it is desired to select locations where the grid is well defined, aiming to avoid interpolation errors. Therefore, the surfaces S_I, S_2, S_S, S_{BN}, S_{CC}, S_{13}, S_{CN}, S_6 and S_P will be used here. The conservation of momentum applied to the captured and post-exit streamtubes leads to the following equation for the standard net thrust [40, 42]

$$T_N = \int_{S_0} \left[\rho u \left(\vec{V} \cdot \vec{n}\right) + (p - p_\infty)\, n_x - (\vec{\tau}_x \cdot \vec{n})\right] dS - \int_{S_{out}} \left[\rho u \left(\vec{V} \cdot \vec{n}\right) + (p - p_\infty)\, n_x - (\vec{\tau}_x \cdot \vec{n})\right] dS \tag{38}$$

where S_{out} includes all the surfaces wetted by the exhaust jets. Note that the standard net thrust as presented in Eq. (38) is also referred to as "modified standard net thrust" [44], since the forces acting on the external core cowl and plug surfaces are included on it. The configuration drag can then be written as

$$D_c = F_N - T_N \tag{39}$$

The integrated force on the fan cowl Φ_{FC} can be defined as

$$\begin{aligned} \Phi_{FC} &= \int_{S_{FC}} \left[(p - p_\infty)\, n_x - (\vec{\tau}_x \cdot \vec{n})\right] dS \\ &= \left(\Phi_p + \Phi_f\right)_{S_{FC}} \end{aligned} \tag{40}$$

where Φ_p is the skin pressure force, Φ_f the skin friction force and S_{FC} is the fan cowl surface.

The pre-entry force F_{pre} is defined as

$$F_{pre} = \int_{S_0 \cup S_{in}} \left[\rho u \left(\vec{V} \cdot \vec{n}\right) + (p - p_\infty)\, n_x - (\vec{\tau}_x \cdot \vec{n})\right] dS \tag{41}$$

where S_{in} is comprised of all the inlet surfaces wetted by captured streamtube.

The integrated force on the internal nacelle surfaces S_{scrub}, scrubbed by the pre-entry and post-exit streamtubes, can be referred to as scrubbing force Φ_{scrub} and expressed as follows

$$\begin{aligned} \Phi_{scrub} &= \int_{S_{scrub}} \left[(p - p_\infty)\, n_x - (\vec{\tau}_x \cdot \vec{n})\right] dS \\ &= \left(\Phi_p + \Phi_f\right)_{S_{scrub}} \end{aligned} \tag{42}$$

Moreover, Eq. (36) can be written as follows

$$\begin{aligned} F_N &= \int_{S_{FC} \cup S_{in} \cup S_{out}} \left(\vec{f} \cdot \vec{n} \right) \, dS \\ &= \left(\Phi_p + \Phi_f \right)_{S_{FC}} + \int_{S_{in} \cup S_{out}} \left(\vec{f} \cdot \vec{n} \right) \, dS \\ &= \left(\Phi_p + \Phi_f \right)_{S_{FC}} + F_{pre} - T_N \end{aligned} \tag{43}$$

finally, the configuration drag becomes

$$\begin{aligned} D_c &= \left(\Phi_p + \Phi_f \right)_{S_{FC}} + F_{pre} \\ &= \left(\Phi_p + \Phi_f \right)_{S_{skin}} - \left(\Phi_p + \Phi_f \right)_{S_{scrub}} + F_{pre} \end{aligned} \tag{44}$$

where S_{skin} is comprised of all skin surfaces wetted by the air passing through and outside of the nacelle. Moreover, the drag coefficient, C_D, can be defined by using the fan face area A_{fan} as reference, as follows

$$C_D = \frac{D_c}{0.5 \rho_\infty V_\infty^2 A_{fan}} \tag{45}$$

D. Inlet distortion and mass flow ratio

A reference aerodynamic parameter for the inlet is the mass flow ratio MFR , which is defined as the ratio of the streamtube captured area A_0 and the highlight area A_{hi}. Typical values for MFR vary between 0.7 and 0.8 at cruise and are greater than unity for low speed conditions.

At high angle of attack or crosswind, boundary layer separation can occur internally in the inlet and distortion can be severe. A common parameter used to assess the distortion level is the DC_{60} coefficient, defined as

$$DC_{60} = \frac{\overline{P}_{02} - \overline{P}_{02,60}}{\overline{q}} \tag{46}$$

where $\overline{P}_{02}$ and $\overline{q}$ are the area averaged total and dynamic pressures at the fan face, and $\overline{P}_{02,60}$ is the area averaged total pressure at the most distorted 60-degree circumferential sector at the fan face.

E. Operating Conditions

During the preliminary design phase of nacelles, it is not practical to consider all the segments existent in an aircraft mission, due to the computational costs of 3D CFD simulations. Therefore, the operating conditions chosen for the present study are the ones considered to be the most critical for the engine's performance and to impose limitations to the nacelle's design [12]. A summary of the operating conditions is presented in Table 5.

The different operating points and why they are considered critical for the nacelle and engine performance, are

Table 5 Critical operating conditions for the design of nacelles

Condition	M	Altitude (m)	AoA (^{o})
Cruise	0.8	10668	5
Wing $C_{l_{max}}$	0.25	4267.2	29
Take-off rotation	0.25	0	17
Crosswind[a]	0.0442	0	0

[a] The crosswind angle (yaw) is 90 degrees.

described next. At cruise, the main goal is to attain low drag, therefore shock-waves shall be avoided when possible and the maximum Mach number M_{max} should be limited. The engine is usually subjected to a local angle of attack (AoA) approximately equal to 5 degrees, caused by the combination of the wing upwash and the aircraft AoA. Under the wing maximum lift coefficient $C_{L_{max}}$ condition, the aircraft is subjected to the largest angle of attack which is allowed in flight. Although it is not typically encountered in the flight mission, it is important for the certification procedure [12]. In this case, the main concerns are internal inlet separation and distortion levels at the fan face. The take-off (TO) rotation condition occurs at the end-of runway when the aircraft nose is pitching up. Inlet separation and high distortion are also the major problems, since the engine is subjected to relatively high incidence. Aircraft certification requires safe and stable operation at takeoff and landing under 90-degree crosswinds, for a wind velocity of at least 20 knots [45]. When subjected to crosswind, inlet flow separation can occur, leading to high levels of distortion and possibly to fan surging. Therefore, crosswind components must be considered during the nacelle design procedure.

F. Design Procedure

The previously described methods were coupled together to create an integrated design framework comprised of engine cycle calculation, parametric geometry generation, automatic multi-block mesh generation, 3D RANS CFD computations and aerodynamic performance evaluation. Figure 8 summarizes the overall nacelle design procedure, which is applicable for both ultra-short and conventional length nacelles.

The first step is to perform the design point (DP) cycle calculation for the engine whose nacelle will be designed. The DP selected for this work was mid-cruise. Afterwards, the operating point of interest is defined and, in case it consists of an off-design operating condition, the off-design point (ODP) cycle calculation is performed. To fulfill this first step, the commercial software GASTURB is used.

Next, the DP output data is used together with the geometry input parameters to shape the nacelle using an in-house MATLAB code, built based on the CST method. A multiblock structured mesh is automatically generated by using the software ANSYS ICEM CFD. Furthermore, the solver ANSYS FLUENT is used to perform 3D RANS CFD calculations. The operating point cycle data are used to define the boundary conditions, together with the method described in section II.B.3.

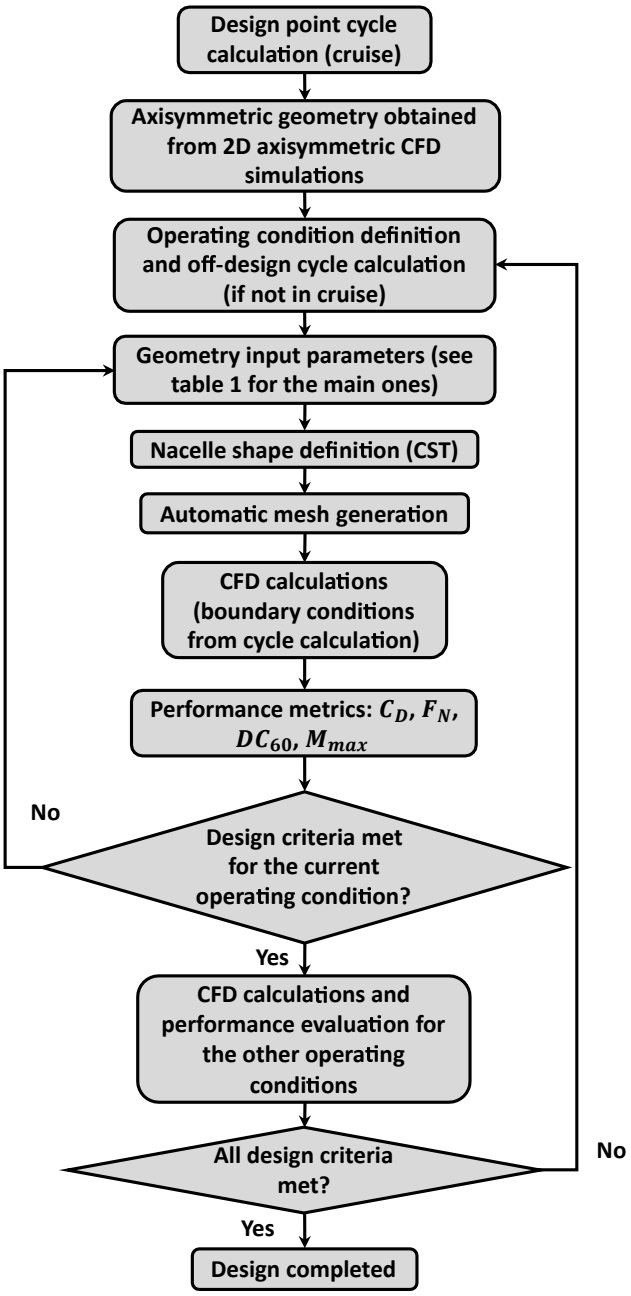

Fig. 8 Flowchart of the design procedure.

The CFD results are post-processed and the nacelle's aerodynamic performance is evaluated. In case the design criteria, defined later in this paper, are not met, new geometric input parameters are defined, and the process is reiterated for the particular operating condition until convergence is achieved. The CFD simulations are performed for all the other operating conditions. In case the design criteria are not met for some operating condition, new geometric input parameters are defined and the process is reiterated, firstly for the current operating point, and lastly for the remaining operating conditions.

The design process can be laborious and time demanding, especially due to the high computational time necessary to fulfill all the steps. Therefore, it is of paramount importance for the aerodynamic designer to understand well the flow field behavior and which parameters play a major role on the nacelle's aerodynamic performance, so that the number of iterations can be minimized. For this work the chosen operating conditions were described in section II.E and summarized in Table 5. The design criteria for the present paper is a M_{max} not higher than 1.2 at cruise, to limit the strength of the shock waves formed on the fan cowling, and, for the other conditions, a DC_{60} lower than 0.05, to assure that the flow will be mostly attached to inlet's internal surface. The choice of M_{max} as a design criterion is in line with Ref. [12]. The value of DC_{60} might seem excessively low, however, it was selected to avoid boundary layer separation, based on the results presented in [17, 46]. For engine certification sake, higher distortion limits could be set. Table 6 shows the design criteria used for each of the chosen operating conditions.

Table 6 Design criteria for the different operating conditions

Condition	Criterion
Cruise	$M < 1.2$
Wing $C_{l_{max}}$	$DC_{60} < 0.05$
Take-off rotation	$DC_{60} < 0.05$
Crosswind	$DC_{60} < 0.05$

III. Results and Discussion

This section is divided in A) mesh independence study; B) Validation of the modified parallel compressor theory; C) thorough analysis of the flow field and of the design variables for each one of the operating conditions and D) discussion regarding the possible design options and choices.

A. Mesh Independence Study

A mesh independence study was carried out to ensure that the selected grid was fine enough to compute the variables of interest. The study was conducted for 8 grids with increasing resolution, for an asymmetric nacelle operating at the cruise condition, shown in Table 5. The number of cells N varied from approximately 3.1×10^6 for the coarsest mesh to 63.6×10^6 for the finest. To guarantee a consistent mesh refinement, a global scaling factor was applied to the entire domain, increasing the number of nodes in all directions. The height of the wall adjacent cells was kept constant across the entire domain, ensuring y^+ below unity, however, the number of cells defining the boundary layer change with the global scaling factor. The results of the grid independence study are shown in Fig. 9 for C_D and F_N. A monotonic behaviour of both C_D and F_N can be observed for the four finest meshes, referred to as grids 1 to 4, from coarsest to finest, as depicted in Fig. 9.

To estimate the exact solution, a generalized Richardson extrapolation with fixed order was employed to grids 3 and

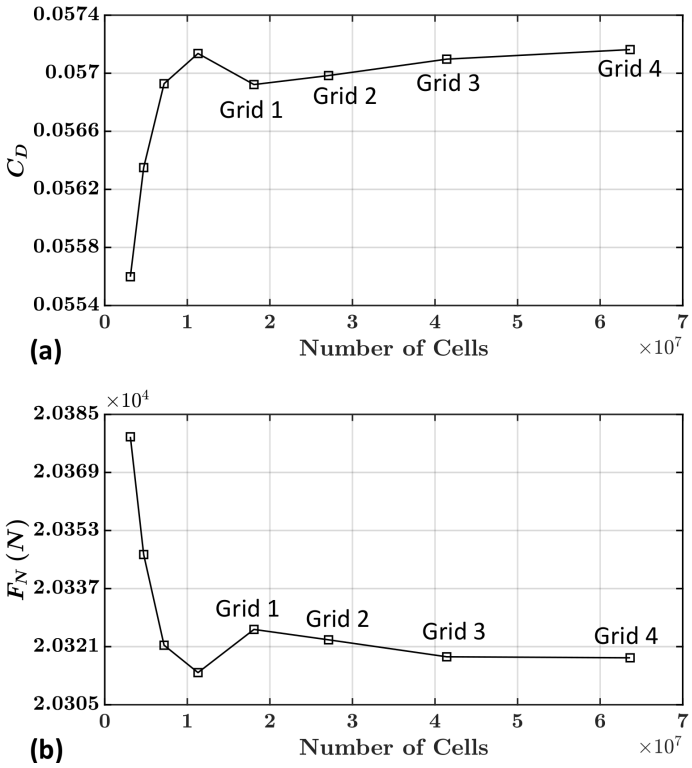

Fig. 9 Mesh independence study results for: (a) drag coefficient C_D, and (b) net propulsive force F_N.

4, by dropping the high order terms (see Ref. [47]). By assuming second order accuracy, the extrapolated values are 0.05736 for C_D and 20317.08 N for F_N. An estimate of the relative error ϵ for a parameter of interest can be found by the difference between an extrapolated value f_e and that evaluated from a discrete solution f_h, for a equivalent mesh size h, as follows

$$\epsilon = \frac{f_e - f_h}{f_e} \tag{47}$$

Figure 10 shows the estimated error of C_D as a function of the equivalent mesh size (in logarithmic scale), where $h = N^{-1/3}$ for a mesh with N elements. The varying order of accuracy is possibly due to grid stretching, non-linearities in the solution, presence of shocks, among others. Grid 1, with approximately 18.07×10^6 elements, was selected for performing the CFD simulations presented later in this paper, since the estimated relative errors were 0.77% for C_D and 0.042% for F_N.

In addition, a domain independence study was carried out for four different domain sizes, namely $50d_{fan}$, $60d_{fan}$, $70d_{fan}$, and $80d_{fan}$. The largest difference in C_D was observed between the $50d_{fan}$ and $80d_{fan}$ domain sizes, being 0.017%. The $60d_{fan}$ domain size was selected used for the test cases presented later in this work, since it presented a 0.004% difference relative to the $80d_{fan}$ domain size.

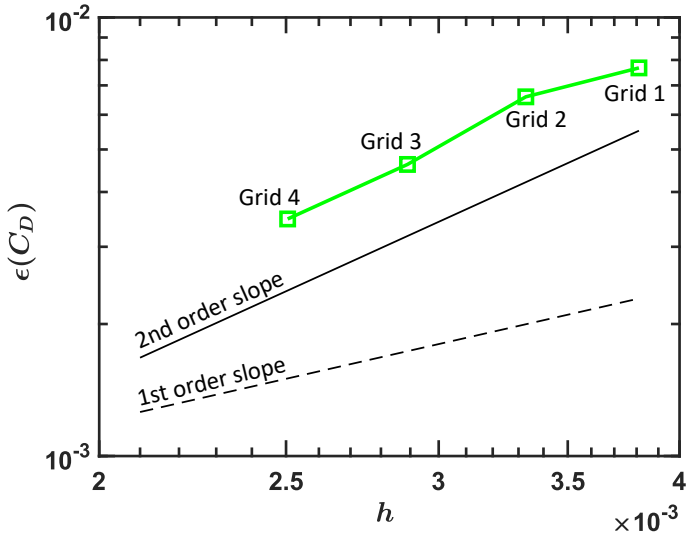

Fig. 10 Estimated relative error of C_D as a function of the equivalent mesh size, in logarithmic scale.

B. Validation of the modified parallel compressor method

In order to verify the validity of the developed method, a test case was carried out for a high-speed fan ingesting a radially distorted flow, and compared with the results obtained from the modified parallel compressor (MPC) method for the same flow conditions. The fan geometry, referred to as daVinki, was provided by GKN Aerospace Engine Systems and used to conduct the current study. The daVinki fan is part of a geared turbofan configuration with bypass-ratio and fan pressure ratio FPR of approximately 15 and 1.39 at mid cruise, respectively. It comprised of a nacelle, 17 rotor blade rows and 43 outlet guide vanes (OGV) blade rows. Further details regarding the design and optimization of the daVinki fan can be found in Ref. [48]. The CFD simulations were conducted using the commercial solver ANSYS FLUENT. Figure 11 shows the computational domain used for the validation cases: (a) for the daVinki fan and (b) for the the MPC method. The daVinki computational domain is split into four parts: nacelle, fan, splitter and OGV, as depicted in Fig. 11a. The fan zone is defined as a rotating domain with rotational speed of 1916 rpm, whilst all the other zones are stationary. All the wall boundaries were defined as no-slip walls. The spinner was defined as a rotating wall and the fan shroud as a counter-rotating wall. The mixing planes were positioned upstream and downstream of the fan and upstream of the OGV blades, as pointed in Fig. 11a. Circumferential periodicity is set at the lateral boundary surfaces. A total pressure profile and a constant total temperature are set at the inlet, whilst at the intermediate compressor (IPC) entry and OGV outlet the static pressure is set with radial equilibrium distribution. The MPC domain extends from the nacelle inlet to a surface defined by the area swept by the fan leading edge, as shown in Fig. 11b. For the inlet, spinner and nacelle, the same conditions described for the daVinki fan are employed. At the outlet, a static pressure distribution is defined, which is calculated based on the incoming flow, using the MPC method.

Structured grids were generated for all the daVinki fan zones. The nacelle and splitter meshes, with respectively 202

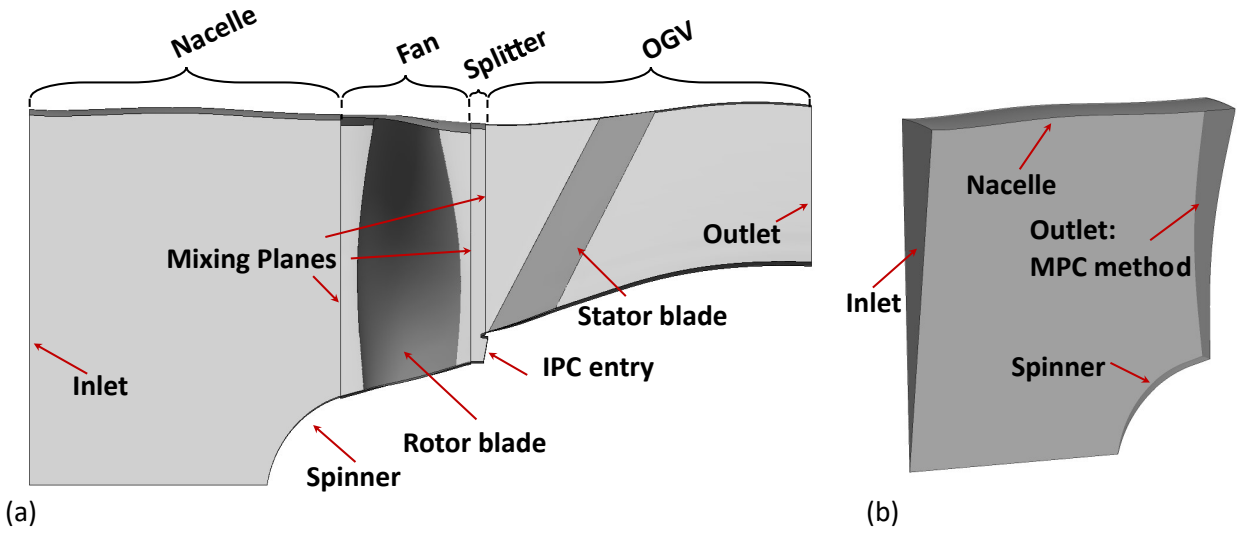

Fig. 11 Computational domain for: (a) daVinki fan and (b) modified parallel compressor method CFD simulations.

and 182 thousand elements, were created using the ANSYS ICEM CFD software, whilst the fan and OGV meshes, with 3.04 and 2.94 million elements, respectively, were generated in ANSYS TURBOGRID. No tip clearance was included. For the MPC domain, a structured grid with approximately 342 thousand elements was created. The wall y^+ was set to be approximately equal to 1 everywhere, for both cases. The turbulence model, fluid type and spacial discretization are the same as used in the nacelle CFD simulations, described in section II.B. The inlet boundary condition was set for an aircraft at cruise for $M = 0.84$ and a flight altitude of 10668 m. To prove that the MPC method is valid for distorted flows, a radial distortion was applied to the upper portion of the inlet boundary, so that the total pressure is constant up to 80% of the inlet radius and then decreases linearly until it reaches 80% of the ambient total pressure, at the nacelle wall. The choice of a purely radial distortion was made so that periodic boundaries could be applied and thus full annulus simulations would not be necessary. At high AoA, the strongest gradient in total pressure occurs radially, therefore, this is deemed to be a representative test case.

As stated in section II.B.3, a speed-line is necessary as an input to the MPC method. It was obtained for the same fan geometry ingesting a clean flow, i.e., with constant total pressure, by gradually increasing the back-pressure at a rotational speed of 1916 rpm. The outlet static pressure was initially estimated by using Eqs. (33) and (34) and then iterated until the mass flow was equal to the one obtained from the daVinki fan simulation. The operating point used for the validation had the following characteristics: $FPR = 1.362$, $BPR = 14.48$ and $\phi_{m,corr} = 195.13\ kg/(m^2 s)$. The speed line obtained from the clean fan simulations was scaled for FPR and η_{is} to the distorted operating point, and then linearized around the same operating point, for consistency with the methodology described in section II.B.3. Figure 12 shows a comparison between the results from the CFD computations for the daVinki fan and the MPC method for (a) total pressure, (b) axial Mach number, (c) static pressure. For the daVinki fan computations, the results were

circumferentially averaged on a surface defined by the area swept by the fan leading edge, and, for the MPC method, the average was taken at the outlet surface. It can be seen, from the static pressure plots, that the MPC reacts to the distorted flow as expected: the fan works harder from approximately 76% of the blade span up to the shroud, where the total pressure and mass flow are lower, consequently the fan face static pressure is reduced, for a constant outlet static pressure. A similar behaviour is observed for the daVinki fan, however, the static pressure reaction to the low momentum portion of the flow starts at about 70% of the blade span and occurs more smoothly, resulting in a lower static pressure reduction, if compared to the MPC method. Thus, it can be stated that the MPC method over-predicts the stabilization capability of the fan, resulting in an abrupter spacial redistribution of momentum. Another clear difference between the two cases is the deceleration occurring in the lower portion of the blade, from the hub to about 30% of the blade span, which is caused by a lower work production near the hub, resulting from the design of the fan blades. The over-prediction in stabilization can be mostly attributed to two reasons: linearization of the speed line, which can over-predict the pressure ratio for low mass flow regions and the usage of a clean speed-line to represent a fan ingesting a distorted flow. The reason for the model not being able to capture the acceleration near the hub is caused by the fact that a single speed-line is being used for the entire blade-span, therefore, radial variations in work caused by the design of the fan blades are not captured.

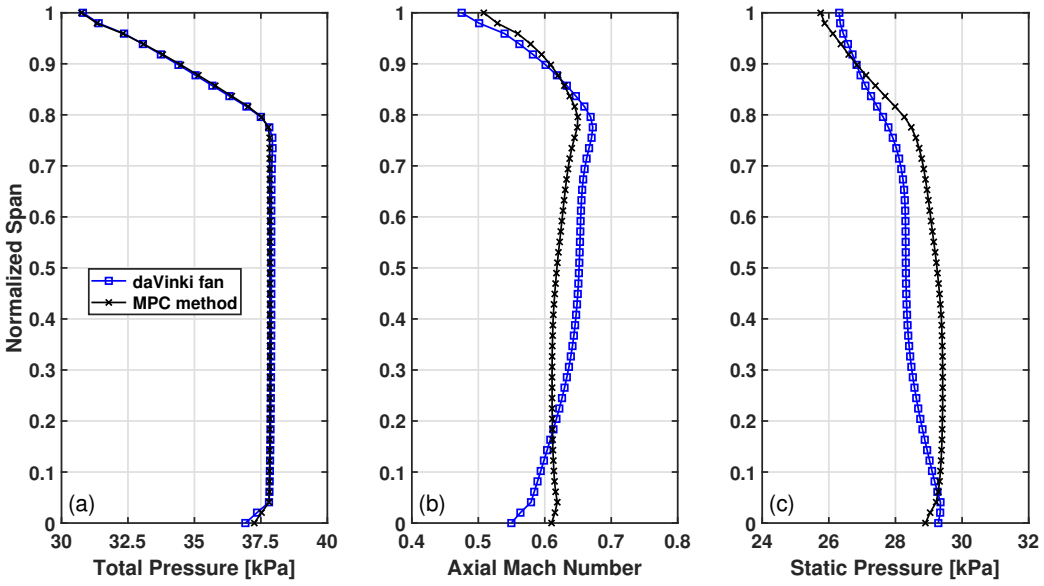

Fig. 12 Comparison between the CFD results obtained for the daVinki fan and the MPC method for: (a) total pressure (b) axial Mach number (c) static pressure. The averages were taken at the fan leading edge position for both cases.

The meridional contours of Mach number for the daVinki fan, MPC method, and constant static pressure at the fan face, are plotted respectively in Fig. 13a, Fig. 13b, and Fig. 13c, for the domain upstream of the fan face. It can be

seen that, both the daVinki fan and the MPC method have the ability of re-accelerating the incoming low momentum flow, when it approaches the fan face. The constant static pressure BC, however, it is not capable of redistributing the momentum to the tip of the blade, thereby, the fan will face an intense drop in Mach number at its upper part, so that the pressure will be constant. Consequently, the flow accelerates over the rest of the blade span, to keep the same averaged mass flow.

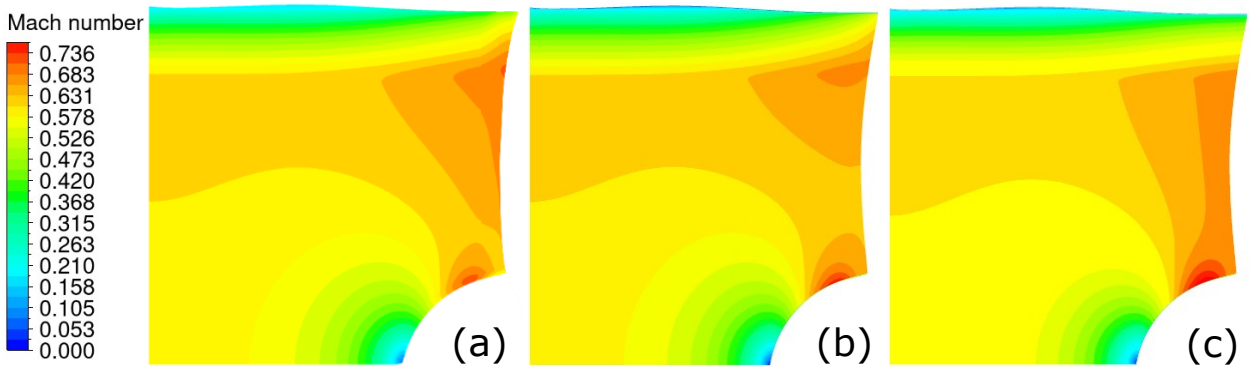

Fig. 13 Comparison between the CFD computations for: (a) daVinki Fan, (b) MPC method, (c) constant static pressure at the fan face.

Although the MPC method is shown to over-predict the fan capability of locally re-energizing distorted flows, it is deemed to be a more appropriate way of representing the fan behaviour than a constant static pressure BC. Due to its simplicity, low computational cost and low amount of necessary input data, the MPC method can be a very useful tool for nacelle designers, since in the early design stages, the fan geometry, as well as detailed performance data, might not be available. Nevertheless, the reader should keep in mind that applying the MPC method as it is might lead to thinner and lower drag nacelle designs than the ones achieved if the fan geometry was used, due to the over-prediction in the flow stabilization. This fact, however, does not conflict with the major goal of this paper, which is to provide good design practices for ultra-short nacelles operating under different flight conditions.

With the penalty of raising the method complexity and number of inputs required, some improvements can be done to the MPC model: 1) using different speed-lines for the blade hub, middle and tip sections, therefore capturing radial variations in work due to the design of the blades; 2) accounting for blockage effects caused by secondary flows in the tip clearance region; 3) modifying the initial clean speed-line to incorporate the effects of distortion. The authors believe that, after these limitations are addressed, the MPC method might be able to provide similar accuracy to more complex and computationally expensive body force models.

C. Design cases

This section provides a discussion on the most important design parameters and challenges encountered in each of the operating conditions described in Table 5. The cases here presented were designed for a future engine with a

mid-cruise bypass ratio of 18, a fan pressure ratio equal to 1.3 and a fan diameter of 2.26 m. For all the cases, the mean L_I/d_{fan} is equal to 0.3. The baseline nacelle for the following studies consists of an axisymmetric geometry with L_{FC}/r_{hi} = 2.96, r_{hi}/r_{max} = 0.87, r_{max}/r_{fan} = 1.19, and r_{te}/r_{hi} = 0.94, which was defined parametrically by conducting several 2D axisymmetric CFD simulations. However, it is out of the scope of this paper to address the initial 2D design.

1. Cruise

Four cases were studied for the cruise condition. The first was an axisymmetric baseline geometry with AoA = 0°. The second was the same geometry but with AoA = 5°. Furthermore, the baseline geometry was drooped using methods 1 and 2, described in section II.A.2. Figure 14 shows the Mach number contours obtained from the 3D RANS computations. The locations where the Mach number is equal to unity are highlighted in white. A strong shock is formed over the fan cowl when the AoA is changed from zero degrees in Fig. 14a to five degrees in Fig. 14b, and the M_{max} increases from 1.028 to 1.394. This is caused by a downward shift in the crown and keel's stagnation point, which forces the flow to accelerate more over the outer part of the crown's lip and over the inner part of the keel's lip. A small region of supersonic flow can also be observed inside the inlet at the keel position.

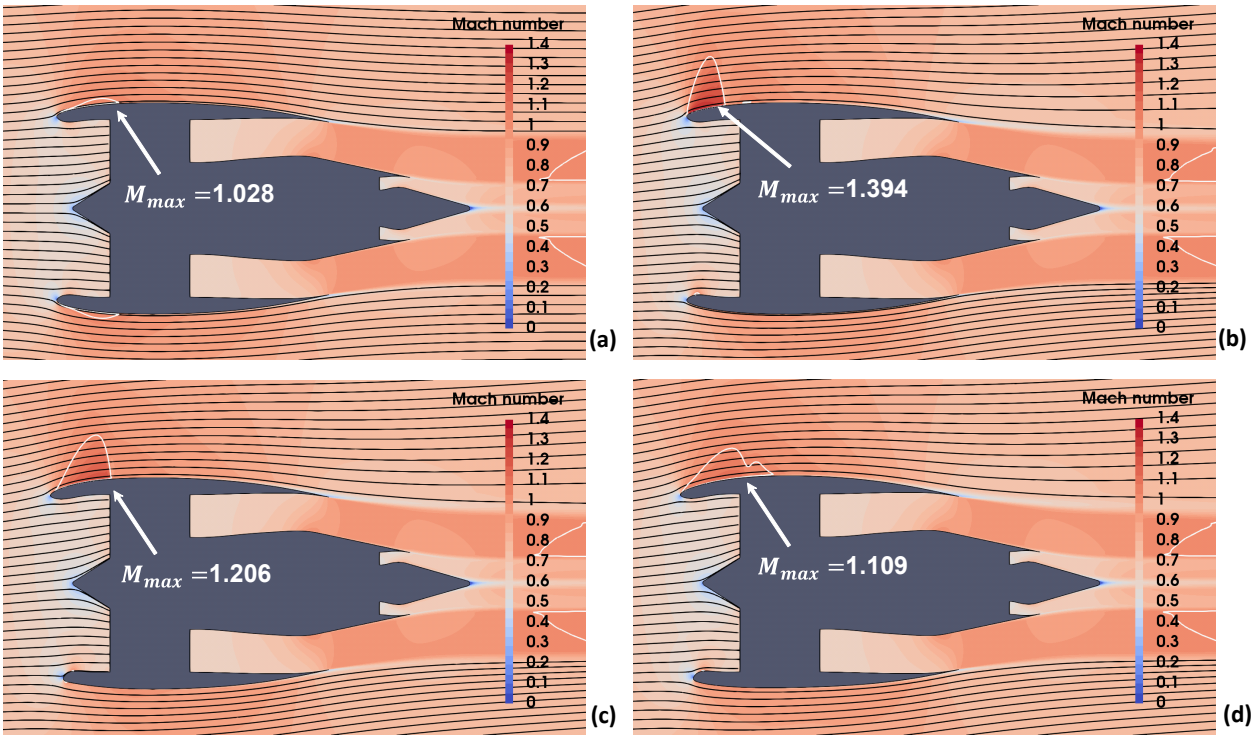

Fig. 14 Mach Number contours at cruise for: (a) axisymmetric nacelle with AoA = 0°, (b) axisymmetric nacelle with AoA = 5°, (c) AoA = 5° and a droop of 4° using method 1, (d) AoA = 5° and a droop of 4° using method 2 .

The results obtained for C_D and M_{max}, for the cases with AoA = 5°, are compared in Table 7. By drooping the

nacelle in four degrees using method 1, the shock strength at the fan cowl is clearly reduced (see Fig. 14b and c). The M_{max} drops from 1.394 to 1.206. The shock is further weakened by using the droop method 2, and M_{max} decreases to 1.109, also for AoA = 5° (see Fig. 14d). Furthermore, C_D was computed for the cases with AoA = 5°, being 0.0580 for the axisymmetric nacelle (Fig. 14b), 0.0574 for the droop method 1 (Fig. 14c), and 0.0569 for the droop method 2 (Fig. 14d). A reduction in drag of 1.0% was achieved by using method 1, and of 1.9% by using method 2, compared to the axisymmetric geometry. The obtained results reinforce the statement that the droop is performed to align the flow with the inlet and reduce drag at cruise.

Table 7 C_D and M_{max} results for the studied cases with AoA = 5°

Case	C_D	M_{max}
Axisymmetric	0.0580	1.394
Droop method 1	0.0574	1.206
Droop method 2	0.0569	1.109

The benefit caused by drooping the inlet can be explained by comparing the 2D nacelle profiles to airfoils. By drooping the crown, as the highlight position moves forward and inwards, the camber angle increases and the incidence between the incoming flow and the mean camber line decreases. For the keel, the local incidence decreases by decreasing the camber angle. The result is that both the mean camber lines are better aligned to the incoming streamlines, occasioning less acceleration around the lip.

The pressure distribution for the crown and the keel are depicted in Fig. 15a and Fig. 15b, respectively, whilst the isentropic Mach number is shown in Fig. 15c, for the crown and in Fig. 15d, for the keel. In Fig. 15a, on the fan cowl, a sudden increase in pressure can be observed for all the cases with AoA = 5°, which occurs just after the shock region. The jump in pressure is the lowest for the droop method 2 case, and the highest for the axisymmetric case, whilst for AoA = 0°, the pressure variation occurs smoothly downstream of the lip. This suggests that the performance improvement achieved by drooping the inlet is manly caused by a reduction in pressure drag.

For the keel, the shocks are very weak or nonexistent on the fan cowl and thus no abrupt changes in pressure are observed (see Fig. 15b). Nevertheless, small zones of intense suction can be observed internally in the inlet, near to its throat. This is caused by a supersonic acceleration region, which can be problematic in case the MFR increases significantly. The droop method 2 was selected to proceed with the nacelle design, since it provided better results, in terms of drag, compared to method 1.

2. Wing maximum lift coefficient

The starting point for the wing $C_{l_{max}}$ operating condition was the geometry generated using the droop method 2, discussed in the previous section. Not surprisingly a highly separated flow on the lower part of the nacelle was obtained as a result of the CFD computations. To solve this problem, it was necessary to camber down the keel and

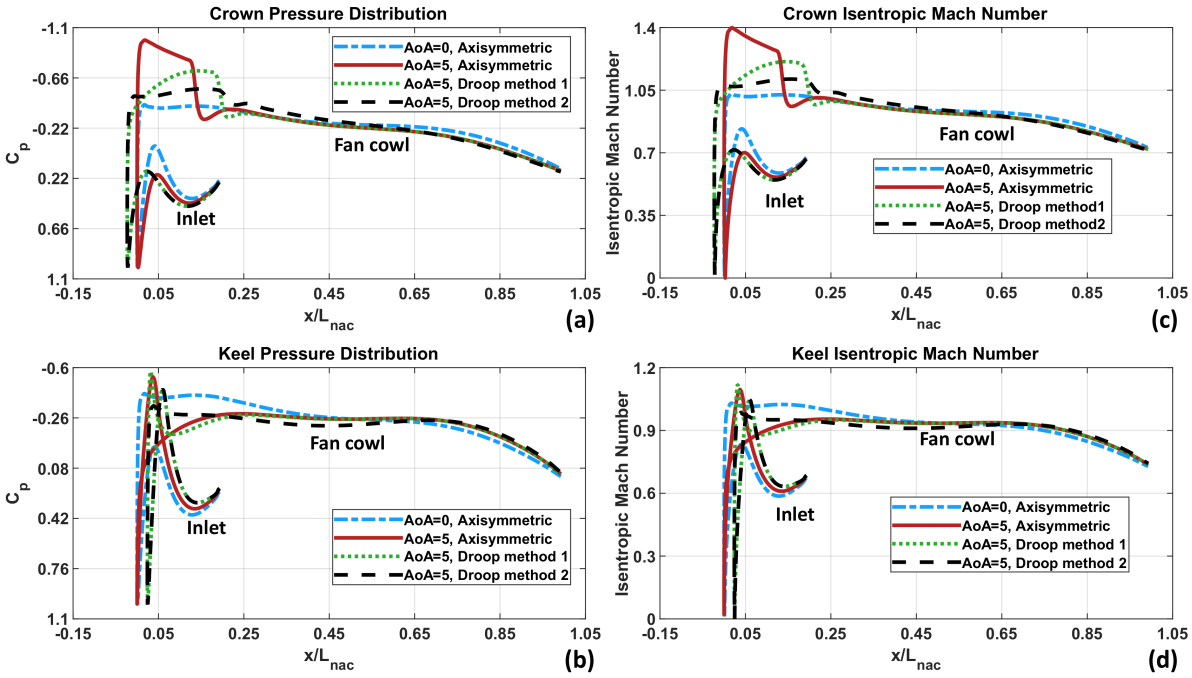

Fig. 15 Pressure distribution at (a) crown, (b) keel and isentropic Mach number distribution at (c) crown, (d) keel for the cruise operating condition .

increase the internal lip thickness. The former solution, similarly to what has already been discussed for cruise, reduces the incidence angle by better aligning the incoming streamlines with the inlet shape. The latter provides a smoother variation in pressure over the inlet and weaker pressure gradients caused by shocks. Moreover, it was found that, for the current operating condition, the lip separation problem can be solved locally on the keel position, without the necessity of reshaping the crown or the MHB profiles.

Six test cases were prepared to show the reader the design parameters which play major role on high incidence operating conditions, and their influence on the flow field. Table 8 shows the main keel design parameters for each case. The non-dimensional leading-edge radius of curvature f_{le} was initially 0.75 for the purely drooped geometry. It was increased to 1.0 to create case CL1. Case CL2 was created by shifting the highlight position downwards, which was achieved by increasing the r_{hi}/r_{max} parameter. Case CL3 was then constructed by raising the lip aspect ratio a/b and hence the throat axial position. Cases CL4 to CL6 were created by modifying singular parameters in case CL3. Case CL4 employed a reduction in contraction ratio r_{hi}^2/r_{th}^2. In CL5 the droop was removed and, finally, f_{le} was decreased to create CL6. The MHB design input parameters were defined as the mean values of the crown and keel ones. Figure 16a shows the keel profiles obtained for cases CL1, CL2 and CL3 and the baseline axisymmetric case, whilst figure 16b depicts the profiles for cases CL3 to CL6.

Figure 17 shows the M contours around the keel's inlet. Due to the high AoA, the stagnation point is moved downwards, over the outer part of the inlet. This requires the streamlines in the vicinity to perform a severe turn over the

Table 8 Main design parameters for the wing $C_{l_{max}}$

Case	r_{hi}/r_{max}	f_{le}	r_{hi}^2/r_{th}^2	a/b	θ_d (^{o})
CL1	0.87	1.0	1.135	2.25	4.0
CL2	0.88	1.0	1.135	2.25	4.0
CL3	0.88	1.0	1.135	5.0	4.0
CL4	0.88	1.0	1.115	5.0	4.0
CL5	0.88	1.0	1.135	5.0	0.0
CL6	0.88	0.75	1.135	5.0	4.0

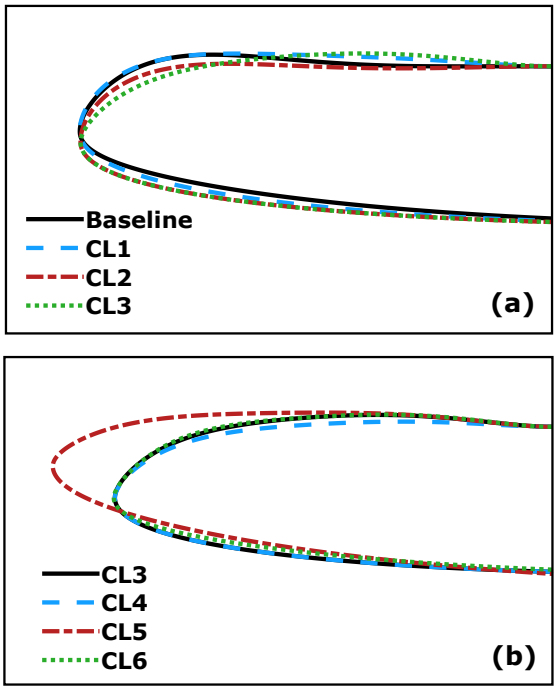

Fig. 16 Inlet keel profiles for the wing $C_{l_{max}}$ cases.

lip (see Fig. 17a) and, as a result, a high acceleration zone is formed downstream of the highlight, inside the inlet. As it can be seen Fig. 17, boundary layer separation occurs for all the cases but CL3. For cases CL1, CL2, shocks are formed in the inner part of the lip, between the highlight and the throat, and boundary layer separation occurs just downstream of them. For cases CL4 and CL5 the shocks occur in a small region at the highlight's proximity and are followed by severe adverse pressure gradients, causing separation to happen instantaneously. In case CL3, a strong shock is formed on the inner lip, however, the change in curvature is smooth enough to prevent an excessively strong pressure gradient. Consequently, the boundary layer remains attached. In case CL6, the reduction in f_{le} causes more abrupt curvature gradients to be followed by the streamlines, resulting in a shock induced separation downstream of the highlight.

It is interesting to notice that drooping the nacelle not only reduced the drag at cruise but also played a fundamental role in avoiding separation at the wing $C_{l_{max}}$ condition. Literature suggests that the major reason for drooping the inlet

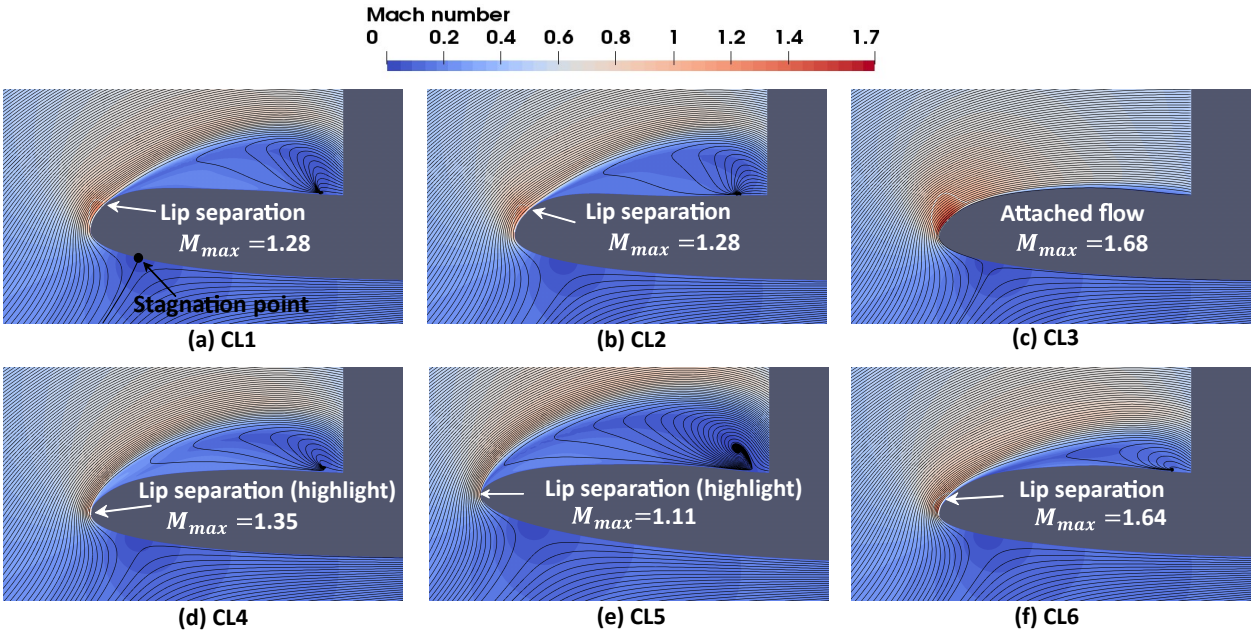

Fig. 17 Mach number contours for cases (a) CL1 (b) CL2 (c) CL3 (d) CL4 (e) CL5 (f) CL6 .

is to improve the aerodynamic performance at cruise and that its effects at low speed conditions are merely marginal [22, 49]. On the contrary, for the particular case studied, droop has shown to be highly beneficial for both cases, as it can be observed by comparing Fig. 17 (c) and Fig. 17 (e).

The keel pressure and isentropic Mach number distributions for cases CL1, CL3 and CL4 are plotted in Figure 18a and 18b, respectively. It can be seen that, the pressure rise is the steepest for the case CL4, where separation starts just downstream of the highlight and the smoothest for the attached case, CL3. The pressure gradients in CL1 are not as severe as in CL4, although strong enough to cause lip separation.

The values of MFR and DC_{60} are presented in Table 9. As expected, distortion is very low for case CL3, where the flow is attached. Case CL5 presented the highest levels of distortion. Furthermore, the computed MFR values are typical for the current operating condition [12]. The DC_{60} values were compared to the ones found in [17, 46], and they are similar for both fully attached and highly separated cases.

Table 9 MFR and DC_{60} results for the studied cases

Case	MFR	DC_{60}
CL1	1.5049	0.0964
CL2	1.4884	0.0839
CL3	1.4880	0.0182
CL4	1.4873	0.0884
CL5	1.4896	0.1567
CL6	1.4869	0.0753

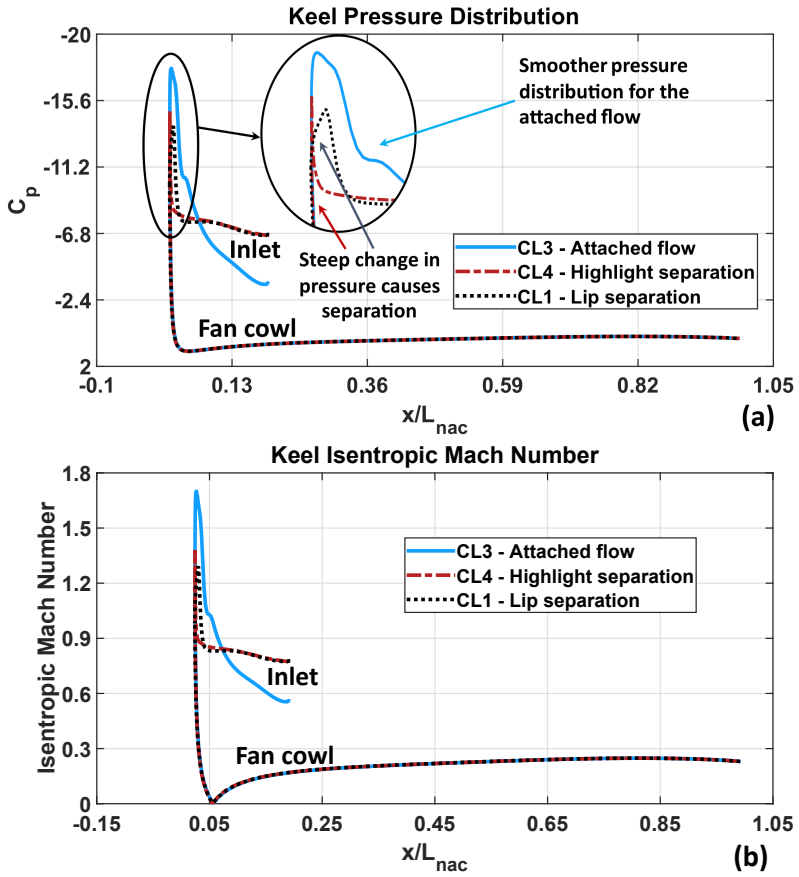

Fig. 18 Keel Pressure distribution (a) and isentropic Mach number (b) for cases CL3, CL5 and CL6.

3. Takeoff Rotation

The same geometry from case CL3 was tested for the take-off rotation condition. The M contours from the CFD computations are shown in Fig. 19. No evident problems with the flow field were detected. Some acceleration can be observed in keel's inner lip, however the flow never reaches supersonic velocities. The computed MFR was equal to 1.41 and DC_{60} to 0.0063.

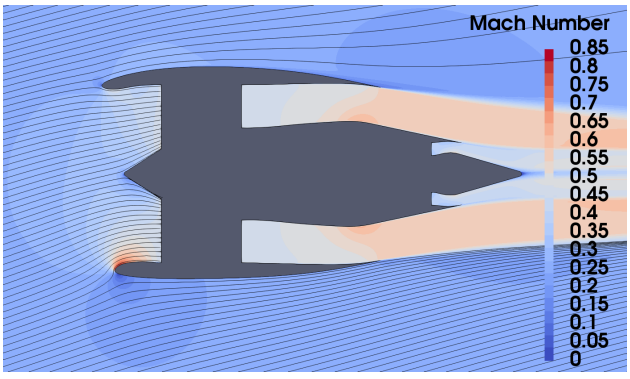

Fig. 19 Contours of Mach number for the TO rotation operating condition.

4. Crosswind

Different than expected, the crosswind separation problem could not be solved by simply employing a local change in geometry on the MHB position. In fact, for the most severe cases, the separation zone can extend from a region leeward of the keel to a position leeward of the crown, covering more than 180 degrees of the nacelle annulus. Therefore, to achieve a separation-free design, a severe shape modification had to be performed both in the crown, MHB and keel positions.

Three test cases were settled in order to elucidate how the main design parameters impact the inlet separation and distortion under the crosswind condition, referred to as CW1, CW2 and CW3. Figure 20 shows the inlet profiles for the: (a) crown, (b) keel and (c) windward MHB. The case CW1 consists of the same geometry presented in CL3, but now under the crosswind condition. For the case CW2, the following modifications were applied: The crown f_{le} and contraction ratio were increased by 20% and 4.9%, respectively. For the keel, the contraction ratio, r_{hi}/r_{max} and r_{max}/r_{fan} were increased by 3.4%, 0.6% and 2.5%, respectively. Also, increases of 25.7% in f_{le}, 10% in contraction ratio, 1.26% in r_{max}/r_{fan}, and a decrease of 39% in lip aspect ratio were performed for the MHB. Note that, despite of a lower lip aspect ratio, the axial position of the throat is moved downstream, since the lip height is greater. For case CW3, the keel and the MHB were kept the same as CW2, whilst a 33% increase in f_{le}, 5% increase in contraction ratio and 47% decrease in lip aspect ratio were employed to the crown. The design parameter values used in each of the crosswind cases are shown in Table 10. Note that changing the parameter r_{max}/r_{fan} is rather undesirable, since it increases the nacelle thickness and hence skin friction drag and weight. Nonetheless, it was necessary to provide a rounder lip, with a smother change in curvature, at the same time as cambering outwards the keel and MHB.

Table 10 Major design parameters used for the crosswind test cases

	CW1				CW2				CW3			
	f_{le}	$\frac{r_{hi}^2}{r_{th}^2}$	$\frac{r_{max}}{r_{fan}}$	a/b	f_{le}	$\frac{r_{hi}^2}{r_{th}^2}$	$\frac{r_{max}}{r_{fan}}$	a/b	f_{le}	$\frac{r_{hi}^2}{r_{th}^2}$	$\frac{r_{max}}{r_{fan}}$	a/b
Crown	0.75	1.135	1.19	2.25	1.2	1.25	1.19	1.9	0.9	1.19	1.19	2.25
MHB	0.875	1.135	1.19	3.625	1.1	1.25	1.205	2.2	1.1	1.25	1.205	2.2
Keel	1.0	1.135	1.19	5.0	1.0	1.175	1.22	5.0	1.0	1.175	1.22	5.0

Fundamentally, lip separation under crosswind is avoided the same way as in the wing $C_{l_{max}}$ condition: by better aligning the local streamlines with the inlet mean camber line and by providing a smooth change in curvature over the fluid's path. The difference is that now the phenomena is far more three-dimensional than before and cannot be solved merely by local geometry adjustments.

Figure 21 shows the total pressure contours plotted on the fan face and on the iso-surface of zero axial velocity for the studied cases. The latter represents the boundary surface of the separated zone. It can be noticed that a large separation zone, covering more than 180 degrees of the nacelle annulus, is formed in case CW1. The separation zone

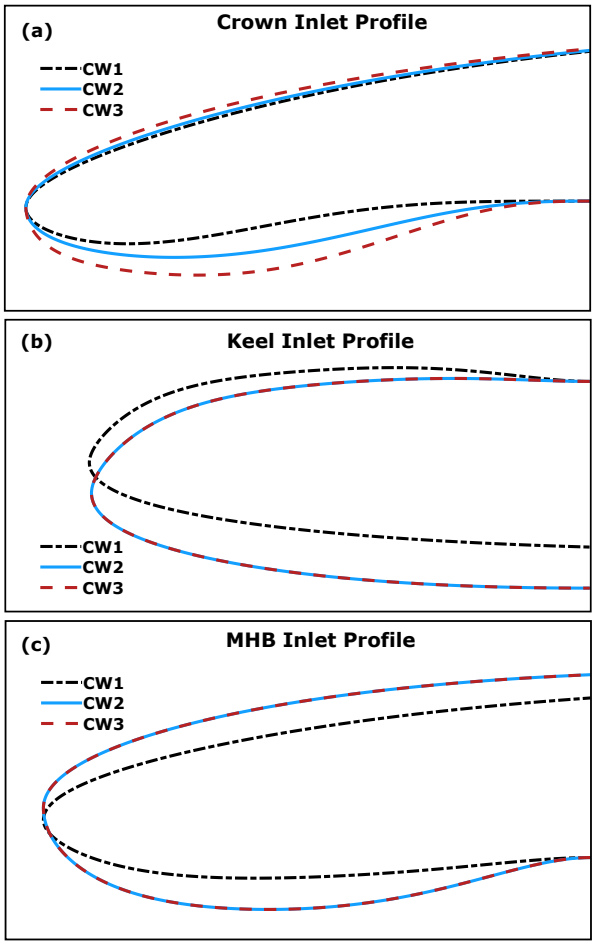

Fig. 20 Inlet profiles for the (a) crown, (b) keel and (c) windward MHB.

area was decreased in CW2, covering only the upper part of the inlet, and vanished completely in CW3.

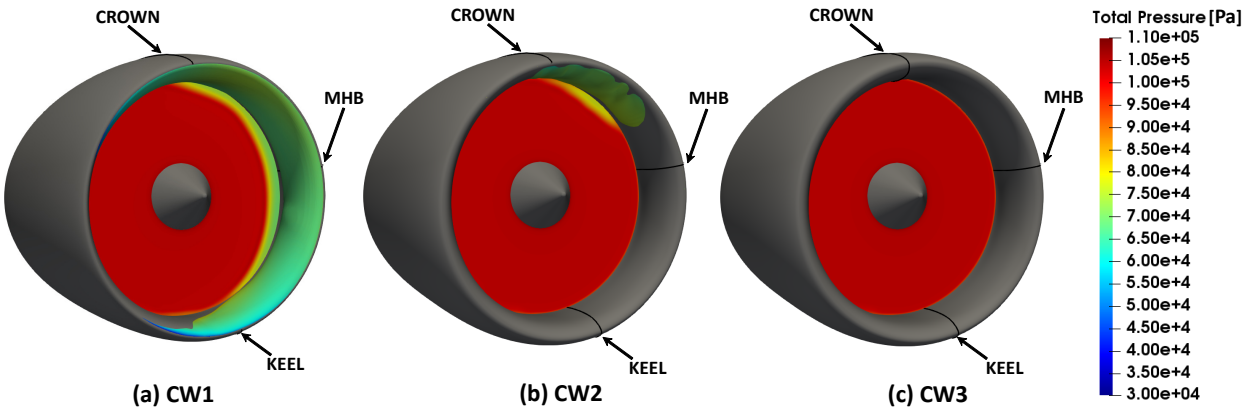

Fig. 21 Total pressure contours plotted on the separation zone, represented by the iso-surfaces of zero axial velocity, for cases (a) CW1 (b) CW2 (c) CW3. The iso-surfaces were restricted to the internal part of the inlet. No boundary layer separation was detected in case CW3.

Table 11 shows the computed MFR, DC_{60} and M_{max} for the crosswind simulations. In case CW1 and CW3, DC_{60} was computed by using a 60-degree sector sweeping the most windward position at the fan face, extending circumferentially 30 degrees above and 30 degrees below the MHB. For the case CW2, however, the sector was rotated in 55 degrees to cover the mostly distorted area. The high values of MFR are caused by high engine mass flows and very low speeds, causing the stream-tube captured area to be extremely large. DC_{60} is the highest in case CW2, because, although the separation area is smaller than in CW1, it imposes a larger local loss in total pressure. For CW3, where the boundary layer is fully attached, the DC_{60} value is very low, as expected.

Table 11 Crosswind results

Case	MFR	DC_{60}	M_{max}
CW1	7.0856	0.1567	1.222
CW2	6.8876	0.1604	1.486
CW3	6.8890	0.0025	1.501

The isentropic Mach number M_{is} distributions are plotted in Fig. 22, on the crown, MHB and keel positions, for the studied cases. A similar behavior to the wind $C_{l_{max}}$ is observed, where the steeper the drop in M_{is}, and hence the raise in static pressure, the more prone to separation the flow is. Particularly for the MHB in cases CW2 and CW3 two successive shock were detected, the first being strong and the second weaker, as depicted in Fig.22c.

D. Design Choices

The geometries presented in cases CL3 and CW3 were selected and tested for the remaining operating conditions. This section brings a comparison between the two designs at cruise and a discussion about the design options which should be considered from now on. Figure 23 shows the M contours for (a) CL3 and (b) CW3. For CL3 the M_{max} is equal to 1.114 and C_D to 0.0572, whilst for CW3 the M_{max} is equal to 1.225 and C_D to 0.0601. The increase in drag from CL3 to CW3 is equal to 5.1%, besides, the fan cowl shocks are stronger and the velocities near the inlet's throat are close to sonic for CW3. Moreover, the constraint in M_{max} of 1.2, established as a design criterion, was not achieved. On the other hand, a fully attached flow was obtained under all the other operating conditions.

The CL3 design is the best for cruise, also behaving well for TO-rotation and wing $C_{l_{max}}$ conditions. However, the flow is highly separated when subjected to crosswind, with relatively high levels of distortion. Although the designs shown in this paper do not represent optimum solutions, they serve as a good indication that some substantial cost in drag should be payed in order to avoid inlet separation.

In face of the aforementioned facts, the aerodynamic designer has two options: The first would be go for the lowest possible drag at cruise and employ active flow control mechanisms, such as blow-in doors, to avoid separation and alleviate distortion. The second would be to pay some price in drag and further iterate on geometry CW3 to reduce the amount of increased drag. Both cases will have some further cost in weight. The former solution would add the

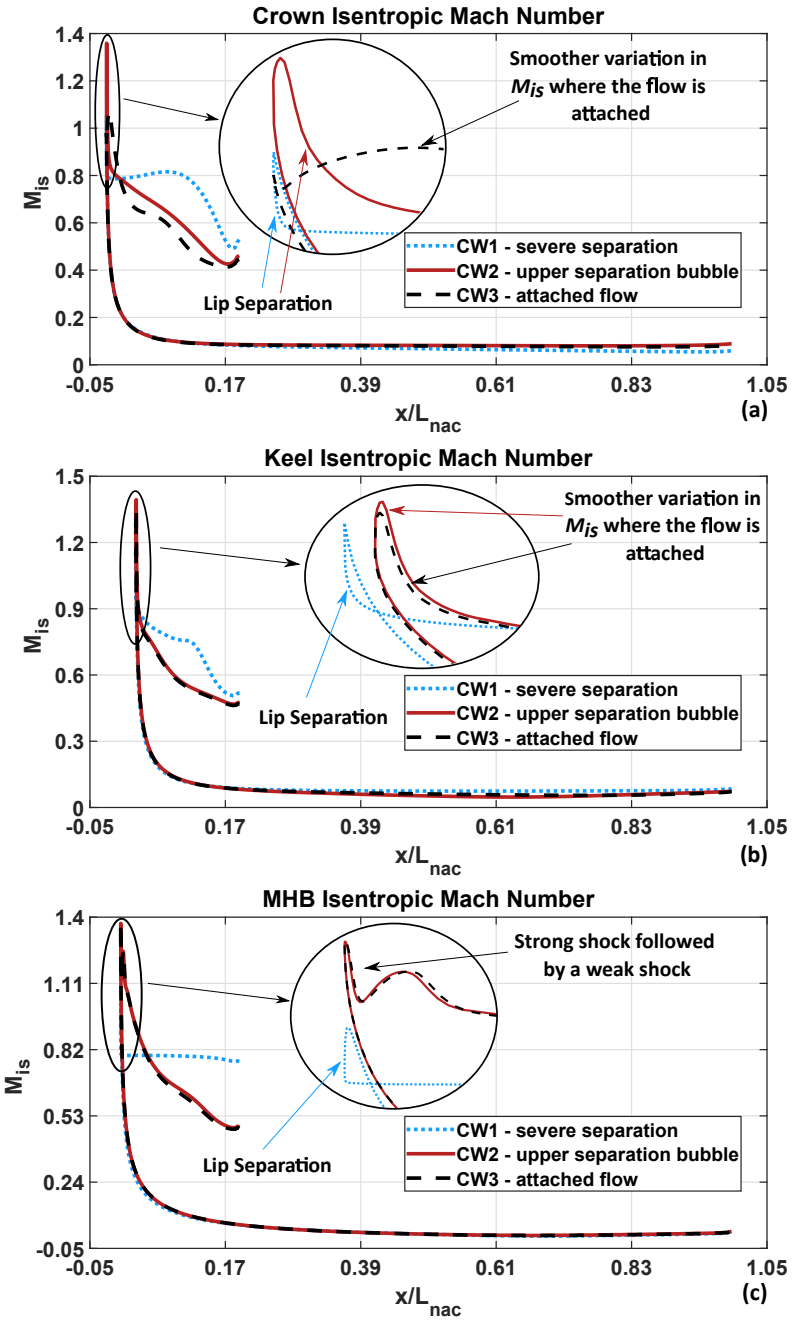

Fig. 22 Isentropic Mach number ploted for the (a) crown, (b) keel and (c) MHB. Steep pressure gradients lead M_{is} to drop and the flow to separate.

weight of the flow control mechanisms, whilst the latter would be heavier due to an increased nacelle thickness. Which decision is the best, however, goes beyond a purely aerodynamic assessment and is out of the scope of the present paper.

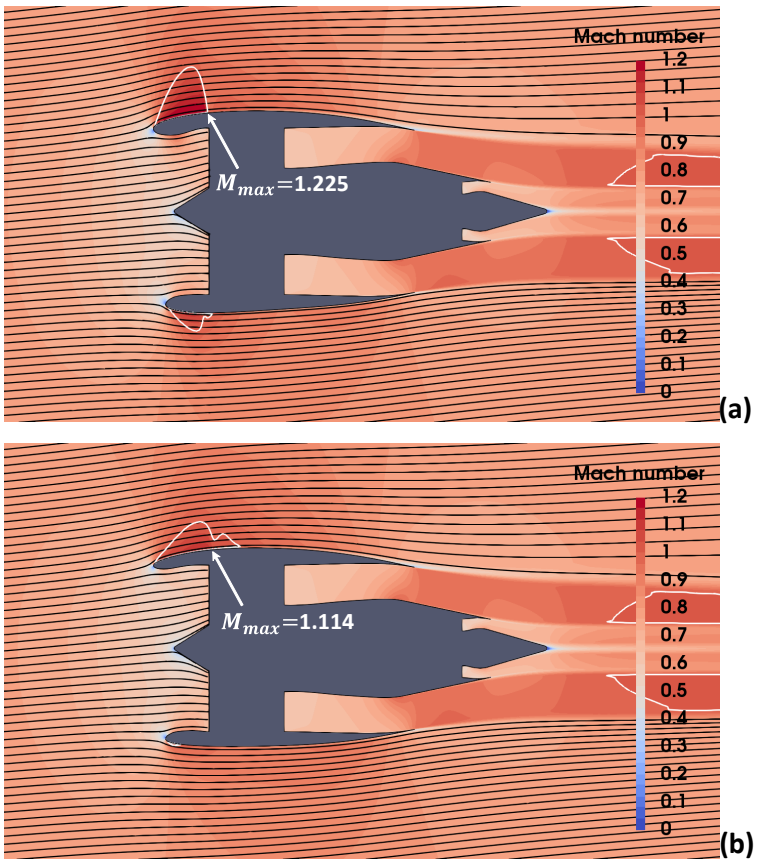

Fig. 23 Contours of Mach number at cruise for the two possible design choices: (a) CL3 and (b) CW3.

IV. Conclusions

A novel methodology for multipoint design of ultra-short nacelles has been developed. The modified parallel compressor method was developed and validated, and it has shown to be able to reasonably predict the fan behaviour, for distorted incoming flows, with low computational cost and few input variables. Several nacelle test cases were presented under different critical operating conditions and a thorough discussion on the flow field behavior was given for them. The most impacting design parameters for each operating condition were highlighted and discussed. Two nacelle geometries were selected and a discussion on different design options was performed.

The major contributions brought by this article are: 1) provide new methods and tools capable of designing ultra-short nacelles which operate well under the most critical aircraft operating conditions, free of strong shocks and of internal inlet separation. 2) Identify the main parameters for the design of ultra-short nacelles and how they affect the flow field.

The major findings obtained with the current research were: 1) drooping the inlet has the potential for weakening shock waves at the fan cowling and reducing drag at cruise, as literature suggests. Moreover, particularly for ultra-short nacelles, it has shown to have a strong impact on high-incidence/low-speed internal inlet separation; 2) Results suggest

that crosswind is the most critical condition among the selected ones, and it requires the nacelle to be drastically reshaped in order to guarantee fully attached flow, leading to a considerable increase in drag at cruise; 3) Each of the operating conditions has its own particularities when it comes to shaping the nacelle, nonetheless, the same fundamental principle can be applied to all of them, which is providing a good alignment of the local nacelle mean camber line with the incoming streamlines, and assuring a smooth change in curvature throughout the path of the streamlines.

Future work should focus on evaluating more integrated geometries, including pylons, wings and fuselage, thus allowing to assess how the interference effects impact the design of ultra-short nacelles.

Funding Sources

This research work was funded by the Swedish National Aviation Engineering Research Program, NFFP, supported by Swedish Armed Forces, the Swedish Defense Materiel Administration, Swedish Governmental Agency for Innovation Systems (VINNOVA) and GKN Aerospace. All the computations were performed using C3SE (Chalmers Center for Computational Science and Engineering) resources, provided by SNIC (Swedish National Infrastructure for Computing).

References

[1] Christie, R., Heidebrecht, A., and MacManus, D., "An Automated Approach to Nacelle Parameterization Using Intuitive Class Shape Transformation Curves," *Journal of Engineering for Gas Turbines and Power*, Vol. 139, No. 6, 2017. https://doi.org/10.1115/1.4035283.

[2] Christie, R., Robinson, M., Tejero, F., and MacManus, D. G., "The Use of Hybrid Intuitive Class Shape Transformation Curves in Aerodynamic Design," *Aerospace Science and Technology*, Vol. 95, 2019, p. 105473. https://doi.org/10.1016/j.ast.2019.105473.

[3] Tejero, F., MacManus, D. G., and Sheaf, C., "Surrogate-based Aerodynamic Optimisation of Compact Nacelle Aero-engines," *Aerospace Science and Technology*, Vol. 93, 2019, p. 105207. https://doi.org/10.1016/j.ast.2019.05.059.

[4] Tejero, F., Robinson, M., MacManus, D. G., and Sheaf, C., "Multi-objective Optimisation of Short Nacelles for High Bypass Ratio Engines," *Aerospace Science and Technology*, Vol. 91, 2019, pp. 410–421. https://doi.org/10.1016/j.ast.2019.02.014.

[5] Stańkowski, T. P., MacManus, D. G., Sheaf, C. T., and Christie, R., "Aerodynamics of Aero-engine Installation," *Proceedings of the Institution of Mechanical Engineers, Part G: Journal of Aerospace Engineering*, Vol. 230, No. 14, 2016, pp. 2673–2692. https://doi.org/10.1177/0954410016630332.

[6] Stankowski, T. P., MacManus, D. G., Robinson, M., and Sheaf, C. T., "Aerodynamic Effects of Propulsion Integration for High Bypass Ratio Engines," *Journal of Aircraft*, Vol. 54, No. 6, 2017, pp. 2270–2284. https://doi.org/10.2514/1.C034150.

[7] Robinson, M., MacManus, D. G., and Sheaf, C., "Aspects of Aero-engine Nacelle Drag," *Proceedings of the Institution of Mechanical Engineers, Part G: Journal of Aerospace Engineering*, Vol. 233, No. 5, 2019, pp. 1667–1682. https://doi.org/10.1177/0954410018765574.

[8] Tejero, F., Christie, R., MacManus, D., and Sheaf, C., "Non-axisymmetric Aero-engine Nacelle Design by Surrogate-based Methods," *Aerospace Science and Technology*, Vol. 117, 2021, p. 106890. https://doi.org/10.1016/j.ast.2021.106890.

[9] Goulos, I., Stankowski, T., Otter, J., MacManus, D., Grech, N., and Sheaf, C., "Aerodynamic Design of Separate-Jet Exhausts for Future Civil Aero-engines—Part I: Parametric Geometry Definition and Computational Fluid Dynamics Approach," *Journal of Engineering for Gas Turbines and Power*, Vol. 138, No. 8, 2016. https://doi.org/10.1115/1.4032649.

[10] Goulos, I., Otter, J., Stankowski, T., MacManus, D., Grech, N., and Sheaf, C., "Aerodynamic Design of Separate-Jet Exhausts for Future Civil Aero-engines—Part II: Design Space Exploration, Surrogate Modeling, and Optimization," *Journal of Engineering for Gas Turbines and Power*, Vol. 138, No. 8, 2016. https://doi.org/10.1115/1.4032652.

[11] Otter, J. J., Christie, R., Goulos, I., MacManus, D. G., and Grech, N., "Parametric Design of Non-axisymmetric Separate-jet Aero-engine Exhaust Systems," *Aerospace Science and Technology*, Vol. 93, 2019, p. 105186. https://doi.org/10.1016/j.ast.2019.05.038.

[12] Peters, A., Spakovszky, Z. S., Lord, W. K., and Rose, B., "Ultrashort Nacelles for Low Fan Pressure Ratio Propulsors," *Journal of Turbomachinery*, Vol. 137, No. 2, 2014. https://doi.org/10.1115/1.4028235.

[13] Schnell, R., and Corroyer, J., "Coupled Fan and Intake Design Optimization for Installed UHBR-engines with Ultra-short Nacelles," *22rd International Symposium on Air Breathing Engines*, ISABE Paper 2015-20034, Phoenix, Arizona, USA, 2015.

[14] Coschignano, A., Babinsky, H., Sheaf, C., and Zamboni, G., "Normal-shock/boundary-layer Interactions in Transonic Intakes at High Incidence," *AIAA Journal*, Vol. 57, No. 7, 2019, pp. 2867–2880. https://doi.org/10.2514/1.J058054.

[15] Trapp, L. G., and da Motta Girardi, R., "Crosswind Effects on Engine Inlets: The Inlet Vortex," *Journal of Aircraft*, Vol. 47, No. 2, 2010, pp. 577–590. https://doi.org/10.2514/1.45743.

[16] Yeung, A., Vadlamani, N. R., Hynes, T., and Sarvankar, S., "Quasi 3D Nacelle Design to Simulate Crosswind Flows: Merits and Challenges," *International Journal of Turbomachinery, Propulsion and Power*, Vol. 4, No. 3, 2019, p. 25. https://doi.org/10.3390/ijtpp4030025.

[17] Lee, K.-B., Wilson, M., and Vahdati, M., "Effects of Inlet Disturbances on Fan Stability," *Journal of Engineering for Gas Turbines and Power*, Vol. 141, No. 5, 2018. https://doi.org/10.1115/1.4042204.

[18] Hall, C., and Hynes, T., "Nacelle Interaction With Natural Wind Before Take-off," *Journal of Propulsion and Power*, Vol. 21, No. 5, 2005, pp. 784–791. https://doi.org/10.2514/1.2848.

[19] Vadlamani, N. R., Cao, T., Watson, R., and Tucker, P. G., "Toward Future Installations: Mutual Interactions of Short Intakes With Modern High Bypass Fans," *Journal of Turbomachinery*, Vol. 141, No. 8, 2019. https://doi.org/10.1115/1.4044080.

[20] Kulfan, B. M., "Universal Parametric Geometry Representation Method," *Journal of Aircraft*, Vol. 45, No. 1, 2008, pp. 142–158. https://doi.org/10.2514/1.29958.

[21] Zhu, F., and Qin, N., "Intuitive Class/shape Function Parameterization for Airfoils," *AIAA Journal*, Vol. 52, No. 1, 2014, pp. 17–25. https://doi.org/10.2514/1.J052610.

[22] Berry, D. L., "The Boeing 777 Engine/Airframe Integration Aerodynamic Design Process," *ICAS Proceedings*, Vol. 19, International Council of the Aeronautical Sciences, Paper 94-6.4.4, 1994, pp. 1305–1305.

[23] Goodmanson, L. T., and Schultz, W. H., "Installation and Integration of Transonic Transport Propulsion Systems," *SAE Transactions*, 1971, pp. 2544–2556. https://doi.org/10.4271/710762.

[24] Albers, J. A., and Miller, B. A., "Effect of Subsonic Inlet Lip Geometry on Predicted Surface and Flow Mach Number Distributions," NASA TN D-7446, 1973.

[25] Toubin, H., Din, I. S. E., and Meheut, M., "Multipoint Aerodynamic High Fidelity Shape Optimization of an Isolated Engine Nacelle," *52nd Aerospace Sciences Meeting*, AIAA Paper 2014-0903, 2014, p. 0903.

[26] Ansys, I., "ANSYS FLUENT Theory Guide: Release 16.2," ANSYS, Canonsburg, Pa, 2013.

[27] Menter, F. R., "Two-equation Eddy-viscosity Turbulence Models for Engineering Applications," *AIAA Journal*, Vol. 32, No. 8, 1994, pp. 1598–1605. https://doi.org/10.2514/3.12149.

[28] Vassberg, J. C., Tinoco, E. N., Mani, M., Rider, B., Zickuhr, T., Levy, D. W., Brodersen, O. P., Eisfeld, B., Crippa, S., Wahls, R. A., et al., "Summary of the Fourth AIAA Computational Fluid Dynamics Drag Prediction Workshop," *Journal of Aircraft*, Vol. 51, No. 4, 2014, pp. 1070–1089. https://doi.org/10.2514/1.C032418.

[29] Levy, D. W., Laflin, K. R., Tinoco, E. N., Vassberg, J. C., Mani, M., Rider, B., Rumsey, C. L., Wahls, R. A., Morrison, J. H., Brodersen, O. P., et al., "Summary of Data From the Fifth Computational Fluid Dynamics Drag Prediction Workshop," *Journal of Aircraft*, Vol. 51, No. 4, 2014, pp. 1194–1213. https://doi.org/10.2514/1.C032389.

[30] Sutherland, W., "The Viscosity of Gases and Molecular Force," *The London, Edinburgh, and Dublin Philosophical Magazine and Journal of Science*, Vol. 36, No. 223, 1893, pp. 507–531. https://doi.org/10.1080/14786449308620508.

[31] Hall, D., Greitzer, E., and Tan, C., "Analysis of Fan Stage Conceptual Design Attributes for Boundary Layer Ingestion," *Journal of Turbomachinery*, Vol. 139, No. 7, 2017. https://doi.org/10.1115/1.4035631.

[32] Thollet, W., Dufour, G., Carbonneau, X., and Blanc, F., "Body-force Modeling for Aerodynamic Analysis of Air Intake–fan Interactions," *International Journal of Numerical Methods for Heat & Fluid Flow*, Vol. 26, No. 7, 2016. https://doi.org/FF-07-2015-0274.

[33] Mao, Y., and Dang, T. Q., "Simple Approach for Modeling Fan Systems With a Computational-fluid-dynamics-based Body-force Model," *Journal of Propulsion and Power*, Vol. 36, No. 5, 2020, pp. 642–654. https://doi.org/10.2514/1.B37742.

[34] Cousins, W. T., and Davis, J., Milt W., "Evaluating Complex Inlet Distortion With a Parallel Compressor Model: Part 1—Concepts, Theory, Extensions, and Limitations," *Turbo Expo: Power for Land, Sea, and Air*, Vol. Volume 1: Aircraft

Engine; Ceramics; Coal, Biomass and Alternative Fuels; Wind Turbine Technology, American Society of Mechanical Engineers, Paper GT2011-45067, Vancouver, British Columbia, Canada, 2011, pp. 1–12.

[35] Davis, J., Milt W., and Cousins, W. T., "Evaluating Complex Inlet Distortion With a Parallel Compressor Model: Part 2—Applications to Complex Patterns," *Turbo Expo: Power for Land, Sea, and Air*, Vol. Volume 1: Aircraft Engine; Ceramics; Coal, Biomass and Alternative Fuels; Wind Turbine Technology, American Society of Mechanical Engineers, Paper GT2011-45068, Vancouver, British Columbia, Canada, 2011, pp. 13–23.

[36] Korn, J. A., "Compressor Distortion Estimates Using Parallel Compressor Theory and Stall Delay," *Journal of Aircraft*, Vol. 11, No. 9, 1974, pp. 584–586. https://doi.org/10.2514/3.60390.

[37] Doyle, M., and Horlock, J., "Circumferential Asymmetry in Axial Flow Compressors," *The Aeronautical Journal*, Vol. 70, No. 670, 1966, pp. 953–957. https://doi.org/10.1017/S0368393100082717.

[38] Freeman, C., and Cumpsty, N. A., "Method for the Prediction of Supersonic Compressor Blade Performance," *Journal of Propulsion and Power*, Vol. 8, No. 1, 1992, pp. 199–208. https://doi.org/10.2514/3.23461.

[39] van Dam, C. P., "Recent Experience With Different Methods of Drag Prediction," *Progress in Aerospace Sciences*, Vol. 35, No. 8, 1999, pp. 751–798. https://doi.org/10.1016/S0376-0421(99)00009-3.

[40] Malouin, B., Gariépy, M., Trépanier, J.-Y., and Laurendeau, E., "Engine Pre-entry Thrust and Standard Net Thrust Evaluation Based on the Far-field Method," *Aerospace Science and Technology*, Vol. 45, 2015, pp. 50–59. https://doi.org/10.1016/j.ast.2015.04.014.

[41] Malouin, B., Trépanier, J.-Y., and Laurendeau, E., "Installation and Interference Drag Decomposition via RANS Far-field Methods," *Aerospace Science and Technology*, Vol. 54, 2016, pp. 132–142. https://doi.org/10.1016/j.ast.2016.04.020.

[42] Destarac, D., and van der Vooren, J., "Drag/thrust Analysis of Jet-propelled Transonic Transport Aircraft; Definition of Physical Drag Components," *Aerospace Science and Technology*, Vol. 8, No. 6, 2004, pp. 545–556. https://doi.org/10.1016/j.ast.2004.03.004.

[43] Tognaccini, R., "Drag Computation and Breakdown in Power-on Conditions," *Journal of Aircraft*, Vol. 42, No. 1, 2005, pp. 245–252. https://doi.org/10.2514/1.8510.

[44] Ministry-Industry Drag Analysis Panel (MIDAP) Study Group, "Guide to In-Flight Thrust Measurement of Turbojets and Fan Engines," AGARDograph No. 237, 1979.

[45] van Es, G., "Crosswind Certification—How Does it Affect You?" National Aerospace Laboratory (NLR) Rept. NLR-TP-2006-324, Amsterdam, May 2006.

[46] Hall, C. A., and Hynes, T. P., "Measurements of Intake Separation Hysteresis in a Model Fan and Nacelle Rig," *Journal of Propulsion and Power*, Vol. 22, No. 4, 2006, pp. 872–879. https://doi.org/10.2514/1.18644.

[47] Roache, P. J., "Perspective: A Method for Uniform Reporting of Grid Refinement Studies," *Journal of Fluids Engineering*, Vol. 116, No. 3, 1994, pp. 405–413. https://doi.org/10.1115/1.2910291.

[48] Lejon, M., "Aerodynamic Design Framework for Low-pressure Compression Systems," Ph.D. thesis, Chalmers University of Technology, Gothenburg, Sweden, 2018.

[49] Stockman, N. O., Yates, D. E., and Crum, T. S., "Nacelle Inlet for an Aircraft Gas Turbine Engine," US Patent 5,058,617, 1991.